Integrating Materials and Manufacturing Innovation (2022) 11:648–674
https://doi.org/10.1007/s40192-022-00288-x

TECHNICAL ARTICLE

Temperature-Dependent Material Property Databases for Marine Steels—Part 3: HSLA-80

Jennifer K. Semple[1] · Daniel H. Bechetti[1] · Wei Zhang[2] · Charles R. Fisher[1]

Received: 14 July 2022 / Accepted: 11 November 2022 / Published online: 23 November 2022

Abstract
Integrated Computational Materials Engineering (ICME)-based tools and techniques have been identified as the best path forward for distortion mitigation in thin-plate steel construction at shipyards. ICME tools require temperature-dependent material properties—including specific heat, thermal conductivity, coefficient of thermal expansion, elastic modulus, yield strength, flow stress, and microstructural evolution—to achieve accurate computational results for distortion and residual stress. However, the required temperature-dependent material property databases of US Navy-relevant steels are not available in the literature. Therefore, a comprehensive testing plan for some of the most common marine steels used in the construction of US Naval vessels was completed. This testing plan included DH36, HSLA-65, HSLA-80, HSLA-100, HY-80, and HY-100 steel with a nominal thickness of 4.76 mm (3/16-in.). This report is the second part of a seven-part series detailing the pedigreed steel data. The first six reports will report the material properties for each of the individual steel grades, whereas the final report will compare and contrast the measured steel properties across all six steels. This report will focus specifically on the data associated with HSLA-80 steel.

Keywords ICME · CWM · SYSWELD · Welding · Material database

Background

The importance of lightweighting in the commercial and military shipbuilding sectors has gained attention in recent decades as a way to increase the performance capabilities of products while also reducing total ownership costs. Over the past decade, the production ratio of thin plate (10 mm [3/8-in.] or less) to thicker plate structures for steel construction at Huntington Ingalls Industries—Ingalls Shipbuilding has risen to over 80% in the Coast Guard's National Security Cutter (NSC) program. Modern naval vessel designs also make greater use of complex panels with inserts and cut-outs, further increasing the fabrication complexity to achieve weight savings while meeting structural requirements. However, European shipbuilding research suggests that 30% of hull fabrication costs can be attributed to re-work and fit-up issues due to distortion [1]. Integrated Computational Materials Engineering (ICME)-based prediction tools can be used to quantify distortions associated with the fabrication process of complex stiffened panels or other lightweight structures. These tools, once validated on selected product forms, could be used to establish recommended fitting, fixturing, welding, and assembly sequencing for optimized distortion control in thin-plate steel construction.

These ICME tools require detailed, reliable databases of temperature-dependent material properties in order to increase the accuracy of calculated distortion and residual stresses in welded metallic structures. Of highest importance to the fidelity of such models are the thermo-physical and thermo-mechanical properties of the material(s) being joined. The properties of note include specific heat, thermal conductivity, coefficient of thermal expansion, elastic modulus, yield strength, and flow stress, from room temperature up to nearly the alloy's melting point. The temperatures associated with on-heating and on-cooling phase transformations and their variation with heating rate, cooling rate, and peak temperature are also important for the prediction of stress and distortion evolution.

✉ Charles R. Fisher
charles.r.fisher73.civ@us.navy.mil

[1] Naval Surface Warfare Center, Carderock Division (NSWCCD), West Bethesda, MD, USA

[2] The Ohio State University (OSU), Columbus, OH, USA

While some of these data exist for the most common US Navy steels, these are generally not suitable for use in high-fidelity welding-focused computational models for several reasons. First, the methods of data generation are inconsistent because the testing was completed over many decades by separate researchers and programs. Also, significant gaps exist in the data, especially at temperatures above approximately 400 °C (~ 750 °F). Additionally, some available data are restricted against public distribution. Finally, the data are, in general, subject to reliability issues because of changes in material fabrication and testing practices that have occurred in the decades since the data were generated. To combat this lack of comprehensive and consistent data, the Lightweight Innovations for Tomorrow (LIFT) project entitled, *Robust Distortion Control Methods and Implementation for Construction of Lightweight Metallic Structures*, was created. Generating pedigreed, temperature-dependent material property databases of US Navy-relevant steels was a key task within the LIFT project. A major portion of the work involved analysis of heat-affected zone (HAZ) microstructures, as this region of rapidly changing microstructure results in significant changes in resultant mechanical properties. These varied HAZ region microstructures of Navy-relevant steels also do not have well-established mechanical property data, especially as a function of temperature and heating or cooling rate.

The testing plan included some of the most common marine steels used in the construction of US Naval vessels; namely DH36, HSLA-65, HSLA-80, HSLA-100, HY-80, and HY-100. HSLA is short for "high-strength low-alloy," whereas HY stands for "high yield." The number designation behind HSLA and HY is the minimum yield strength of the plate material in units of ksi. Current (as of this writing) specifications for these alloys can be found in references [2–4]. Material testing for each of the six steel grades was performed jointly by the Welding Engineering Program within the Department of Materials Science and Engineering at the Ohio State University (OSU) and the Welding, Processing, and Nondestructive Evaluation Branch at the Naval Surface Warfare Center, Carderock Division (NSWCCD). The temperature-dependent material property data was then sent to ESI for adaptation for use in their welding-based, finite element analysis (FEA) software colloquially known as *SYSWELD*.

This report is part of a seven-part series based on the pedigreed steel data. The first six reports (the first two of which are given in [5] for DH36 and [6] for HSLA-65) will focus on establishing the material properties for each of the individual steel grades, whereas the final report will compare and contrast the measured steel properties across all six steels. Raw data files and microstructural images can be found within the *Materials Commons* data repository from the University of Michigan [7].

Approach

Material Testing Program

The material property assessment program was developed through inputs from welding engineers at NSWCCD, researchers at OSU, and modeling experts at ESI. The program focused on generating the types of data required to develop Navy-relevant material databases for use by ESI's commercial software, *SYSWELD*. The raw data could also be adapted for use by other FEA tools, such as MSC's *Simufact Welding* or the welding module for *Abaqus*. Specific data included thermo-physical and mechanical properties of the alloys of interest, from room temperature up to near-melting. Density, heat capacity, thermal conductivity, and coefficient of thermal expansion (CTE) were identified as the most important thermo-physical properties. Mechanical properties of interest included the elastic modulus, yield strength, and flow stress.

Material from a single HSLA-80 steel plate procured to NAVSEA Technical Publication T9074-BD-GIB-010/0300 (Tech Pub 300) [4], was analyzed for this project. The plate was acquired by Huntington Ingalls Industries—Ingalls Shipbuilding (HII–Ingalls) and was nominally 4.76 mm (3/16-in.) thick. The room temperature yield strength and elongation requirements for this plate thickness are 552–758 MPa (80–110 ksi) and 14% in 50 mm (2-in.), respectively [4]. There are no ultimate tensile strength requirements for HSLA-80 plate procured to Tech Pub 300 [4]. The plate conformance certification sheet for the material investigated in this study is given in [7]. A portion of this plate was cut into 610 mm by 305 mm (24-in. by 12-in.) pieces and shipped to both NSWCCD and OSU for determination of temperature-dependent material properties. The authors would like to note that the remaining HSLA-80 plate material is being held at NSWCCD, so any researchers seeking to expand the temperature-dependent material property database in future are encouraged to reach out to the corresponding author (C.R. Fisher). Additionally, the authors recognize the limitation that this dataset is for a single plate of HSLA-80, and does not encompass the entire composition and processing range allowed within the material's specification. However, follow-on work to investigate using computational tools to estimate data for the entire composition range is planned.

Chemical Composition

The chemical composition of the base material was measured at OSU using optical emission spectroscopy in accordance with ASTM E415 [8].

Heat-affected Zone Phase Transformation Analysis

Phase transformations of HSLA-80 as a function of austenitization temperature and cooling rate were assessed via dilatometry. Then, continuous cooling transformation (CCT) diagrams were developed for four regions of the HAZ that are subject to microstructural transformation during welding: the intercritical region (ICHAZ); the low-temperature, fine-grained region (FGHAZ1); the high-temperature, fine-grained region (FGHAZ2); and the coarse-grained region (CGHAZ).

The experimental heating and cooling rates were defined by combining typical low alloy steel production heat inputs (0.4–2.6 kJ/mm [10–65 kJ/in.], as suggested by HII-Ingalls engineers), with analytical heat flow simulations using Sandia National Laboratories' *SmartWeld* program [9]. From these calculations, it was determined that heating rates between 10 and 2000 °C/s and cooling rates between 1 and 200 °C/s (1.8 and 360 °F/s) would provide information covering a sufficiently broad range of phase transformation behavior relevant to both slowly cooled welds (*e.g.*, high heat input welds on thin plate) and rapidly cooled welds (*e.g.*, low heat input welds on thick plate). Peak temperatures for three of the four HAZ regions were selected based on previous work with DH36 [5] and HSLA-65 [6]. Selection of the ICHAZ peak temperature required knowledge of the on-heating austenite transformation temperature range and was therefore performed after the completion of initial heating rate tests. Table 1 shows the full test matrix utilized for HAZ CCT diagram development.

Execution of this test matrix was performed at NSWCCD by employing a Gleeble 3500 thermo-mechanical simulation apparatus to apply the prescribed heating and cooling rates. All targeted temperatures and rates were found to be achieved by the system unless otherwise noted within this document. The Gleeble operates on the principles of resistive heating, conductive cooling through water-cooled fixturing, and rapid (50 kHz) control system feedback to apply precise thermal cycles even at rapid heating and cooling rates that cannot be easily achieved by other apparatus. The Gleeble 3500 system, in combination with the apparatus's standard "Pocket Jaw" setup, used full contact copper grips and cylindrical specimens 70 mm (2.76-in.) in length and 3 mm (0.118-in.) in diameter. A linear variable differential transformer (LVDT)-type contact extensometer was used to measure diametric dilation of the specimens during heating and cooling. All dilatometry specimens were extracted perpendicular to the rolling direction of the plate, and all dilatometry tests were performed in an argon atmosphere. An image of the typical experimental setup for the dilatometry testing was shown previously in the DH36 paper [5].

Thermo-Physical Property Analysis

Specimens were sent to the Thermo-physical Properties Research Laboratory, Inc. (TPRL) in West Lafayette, IN for analysis of thermal diffusivity (α) and specific heat (C_p). Thermal diffusivity was measured using the laser flash method according to ASTM E1461 [10]. Specific heat was measured using differential scanning calorimetry (DSC) methods according to ASTM E1269 [11]. Coefficient of thermal expansion (CTE) was measured from the on-heating Gleeble dilatometry data in two regimes: 150–650 °C (302 to 1202 °F) for the base material microstructure, and 1000–1300 °C (1832–2192 °F) for austenite. No attempt was made to determine CTE during the on-heating transformation. CTE calculations were either performed by linear fitting or by discrete analysis using the dilation data endpoints from each temperature range in conjunction with Eq. 1. The material was assumed to be isotropic.

Table 1 Test matrix for HSLA-80 HAZ CCT diagram development

Test type	Region	Peak temperature, °C (°F)	Heating Rate, °C/s (°F/s)	Soak Time, s	Cooling Rate, °C/s (°F/s)
A_{c1}/A_{c3} Determination	N/A	1200 (2192)	10 (18) 100 (180) 200 (360) 500 (900) 1000 (1800) 2000 (3600)	N/A	N/A
CCT Diagram Development	ICHAZ FGHAZ1 FGHAZ2 CGHAZ	825 (1517) 1000 (1832) 1150 (2102) 1350 (2462)	200 (360)	2	1 (1.8) 5 (9) 10 (18) 25 (45) 100 (180) 200 (360)

$$\alpha_T = \left(\frac{\Delta d}{d_0}\right)\left(\frac{1}{\Delta T}\right) \quad (1)$$

where α_T = Linear coefficient of thermal expansion [°C^{-1}], Δd = Change in specimen diameter over the chosen temperature range [cm], d_0 =Initial specimen diameter [cm], ΔT = Temperature range [°C].

The temperature-dependent density (ρ) was calculated using a theoretical cubic volume element under the assumption of isotropic thermal expansion:

$$\rho(T) = \frac{\rho_0 V_0}{V(T)} \quad (2)$$

where $\rho(T)$ = Density at temperature T [g/cm^3], ρ_0 = Room temperature density provided by TPRL [g/cm^3], V_0 = Room temperature volume of the theoretical cubic element [cm^3], $V(T)$ = Volume of the theoretical cubic element at temperature T [cm^3].

V_0 was calculated assuming a side length equal to the room temperature width of OSU's dilatometry specimens. This value was chosen because it corresponds to the starting gauge length for the dilatometer used to measure thermal expansion. A theoretical cubic volume element was chosen instead of the actual specimen dimensions to subvert potential complications with measuring dimensions that were not directly measured by the dilatometer (*e.g.*, the effect of thermal gradients on measurement of the specimen's longitudinal expansion). V_T was simply calculated by:

$$V(T) = [w(T)]^3 \quad (3)$$

where $w(T)$ = Dilatometer-measured specimen width at temperature T [cm].

This method allowed calculation of the density through the austenite transformation. Finally, thermal conductivity (λ) as a function of temperature is then calculated by using Eq. 4:

$$\lambda = \rho \cdot c_p \cdot \alpha \quad (4)$$

where λ = Thermal conductivity [W/cm-°C], ρ = Density [g/cm^3], c_p = Specific heat capacity [J/g-°C], α = Thermal diffusivity [cm^2/s].

Thermo-Mechanical Property Analysis

Tension testing of the HSLA-80 base material at temperatures between 22 and 1100 °C (72 and 2012 °F) was subcontracted to IMR Test Labs in Portland, OR. Room temperature testing was performed in accordance with ASTM A370 [12], and elevated temperature testing was performed in accordance with ASTM E21 [13]. Specimens were of rectangular cross section with 12.7 mm (0.50 in.) gauge width and approximately 50.8 mm (2.0 in.) gauge length. Testing was performed in strain control mode at target rates of 0.005 min^{-1} prior to yield and 0.05 min^{-1} after yield. Specimen dimensions were the same as used during the DH36 [5] and HSLA-65 [6] testing.

HAZ mechanical properties were measured using the Gleeble 3500 at NSWCCD. Prior to mechanical testing, specimens of the standard dog-bone shape were thermally cycled to generate different initial microstructures based on the results of the CCT diagram development described above. For HSLA-80, as with the other low alloy steels, microstructural analysis indicated that substantially different microstructures formed when the material was cooled at 1, 10, 25, and 100 °C/s (1.8, 18, 45, and 180 °F/s). Because of programmatic time constraints, only a peak temperature of 1350 °C (2462 °F) was applied to the tensile specimens. All specimens were heated in an argon atmosphere, and forced air was used to meet cooling rates of 10 °C/s (18 °F/s) and above. All specimens were cooled to room temperature prior to affixing an extensometer. The specimens were then reheated to the test temperature at a rate of 10 °C/s (18 °F/s) and soaked for 10 s before being pulled to failure in crosshead control mode at strain rates targeting those prescribed in ASTM E21 [13]. The crosshead displacement rate used was 0.30 mm/min (0.012 in/min). It is acknowledged that this is not the most representative method of testing for welding-related applications because the stresses that develop during welding do so rapidly and while the material is cooling and undergoing phase transformations. However, given the programmatic intent of establishing the mechanical behavior of specific microstructures and the need to avoid exposing the extensometer device to damagingly high temperatures, the method of cooling to room temperature and testing after reheating was determined to be an acceptable compromise. In cases where the induced microstructure was stronger than the base material, a second reduced gauge section was machined in the specimen prior to testing to ensure specimen fracture in the region of interest, as done previously for DH36 [5] and HSLA-65 [6].

Thermal cycling and subsequent tensile testing were performed using the apparatus's "Pocket Jaw" setup with minimal contact stainless steel grips used to fixture the specimens. These grips were selected to minimize the longitudinal thermal gradient in the gauge length of the specimens during testing. Graphite foil was inserted between the specimen and the grips to further minimize the thermal gradient. The initial gauge length for the tests varied between 8 and 10 mm (0.31 and 0.39 in.) depending on the specimen geometry. Elevated temperature tests were performed in an argon atmosphere. Preliminary testing as part of the DH36 test program [5] indicated that for this setup, the temperature variation across the initial gauge length was 10 to 30 °C (18–54 °F). The typical experimental setup for the tensile testing was the same as used for DH36 [5] and HSLA-65 [6].

Fabrication of Welded Specimens

Two sets of HSLA-80 plates were welded at HII-Ingalls and sent to OSU for analysis of the base material, weld metal, and heat-affected zone (HAZ) microstructures. One set of plates was welded using the submerged arc welding (SAW) process in a two-sided butt joint configuration and the other set was welded using flux cored arc welding (FCAW) in a two-sided tee-joint configuration. The weldment configurations were the same as used during the DH36 [5] and HSLA-65 [6] testing. Welding parameters for both welds are given in Table 2. These weldments enabled correlation of the HAZ microstructures generated through thermal simulation with those produced by arc welding. The two joint configurations are representative of frequently used thin-plate structural welds: seaming butt joints and stiffener fillet joints. These joint types were also the focus of larger fabrication efforts in other tasks within the greater LIFT project as described in [14].

Microstructural Analysis

To quantify and characterize the microstructures observed in HSLA-80, thermally cycled specimens from the HAZ CCT diagram development were metallographically prepared to a final polish of 0.05 µm using standard techniques and etched by immersion in 4% Picral (4 g picric acid dissolved in 100 mL ethanol) for approximately 10 s followed by immersion in 2% Nital (2 mL nitric acid in 100 mL of ethanol) for 3 to 5 s. Identification and phase fraction measurement of the microstructural constituents in each specimen were evaluated using image analysis through light optical microscopy (LOM) and scanning electron microscopy (SEM). Vickers microhardness testing was also used to determine the hardness of the constituent(s) in each CCT specimen. This analysis facilitated proper CCT analysis, provided phase fraction input for the HSLA-80 material property database, and helped determine which thermal cycles were the most appropriate for application in the mechanical testing portion of the program described above. Additionally, a cross section of both the butt joint and tee joint weldments was analyzed. Specimens were metallographically prepared in the manner described above and characterized using LOM and SEM. Vickers microhardness values at 200 g (7.05 oz.) load were taken from the fusion zone through the HAZ to the base material for both weldments.

The authors acknowledge the difficulties associated with identification and quantification of the micro-constituents associated with low carbon steels and associated weldments, as pointed out in [15–18]. Due to the nature of the program investigating these alloys, only LOM and SEM (paired with microhardness) were utilized for phase analysis. Higher resolution techniques such as transmission electron microscopy (TEM) could have been utilized as well, but other research groups have highlighted the difficulties using such techniques for other low carbon steels and associated weldments [19–22]. Nevertheless, even semi-empirical quantification of the identified micro-constituents is vital to support the predictive weld simulations of this common marine steel, for which a temperature-dependent material database is missing from literature. All assumptions made for phase characterization and quantification of HSLA-80 steel are clearly stated within the discussion section.

Results and Discussion

All reported values without a standard deviation are for a single test. Any experimental precision analysis as it relates to uncertainty quantification should be based on the machine manufacturers reported values and ASTM standards noted in the previous "Approach" section.

Chemical Composition

Table 3 shows the averaged results of three base material chemistry measurements for the HSLA-80 plate, plus the manufacturer's plate certification values (shown in [7]) the NAVSEA Tech Pub 300 HSLA-80 specifications [4], and results from a study conducted as part of a Navy Manufacturing Technology (ManTech) program with the Naval Metalworking Center from the mid-2000s [23]. Hereafter,

Table 2 Nominal welding parameters used to fabricate HSLA-80 butt and tee joints

	Butt Joint	Tee Joint
Welding Process	Submerged arc (SAW)	Flux cored arc (FCAW)
Current (A)	300	200
Voltage (V)	30	27
Travel Speed (mm/s [in/min])	14.8 (35)	6.8–7.6 (16–18)
Heat Input (kJ/mm [kJ/in])	0.61 (15.4)	0.71–0.79 (18–20.3)
Consumable Designation(s)	AWS A5.23 EM12K	AWS A5.20 E71T-1
Filler Wire Diameter (mm [in])	3.2 (0.125)	1.3 (0.052)
Interpass Temperature, Max. (°C [°F])	149 (300)	149 (300)

Table 3 Chemical composition of HSLA-80 plate material (wt.%)

Type	C	Mn	P	S	Si	Ni	Cr	Mo	Cu
Measured Avg	0.040	0.56	0.011	0.001	0.26	0.90	0.67	0.20	1.11
Plate Certificate	0.04	0.56	0.011	0.004	0.26	0.85	0.70	0.20	1.17
	0.04	0.58	0.012	0.004	0.27	0.88	0.70	0.20	1.18
Tech Pub 300 [4]	≤0.06	0.40–0.70	≤0.020	≤0.004	≤0.40	0.70–1.00	0.60–0.90	0.15–0.25	1.00–1.30
CTC [23]	0.05	0.64	0.009	0.022	0.2	0.95	0.85	0.2	1.23

Type	Nb	Al	Ti	As	Sb	V	Sn	N	Fe	CEN [24]
Measured Avg	0.030	0.036	0.001	0.005	0.023	0.003	0.011	0.010	Bal	0.252
Plate Certificate	0.027	0.032	0.001	0.0030	0.0020	0.002	0.009	0.0082	Bal	0.253
	0.030	0.033	0.001	0.0030	0.0020	0.002	0.010	0.0080	Bal	0.257
Tech Pub 300 [4]	0.02–0.06	≥0.015	≤0.02	≤0.025	≤0.025	≤0.03	≤0.03	–	Bal	–
CTC [23]	0.04	0.01	–	–	–	<0.01	–	–	Bal	0.295

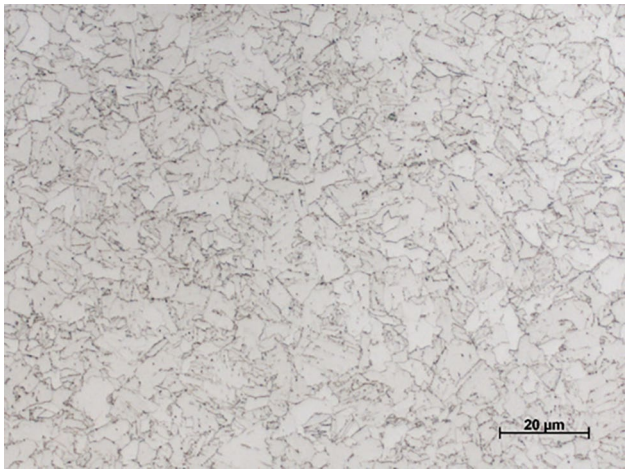

Fig. 1 Representative micrograph of HSLA-80 steel plate base metal microstructure at 1000× magnification using LOM

data from the ManTech study are labeled "CTC" for Concurrent Technologies Corporation, where the testing was conducted. Plate material used in that study was nominally 19.05 mm (0.75-in) thick. As expected, the measured chemical composition values generally agreed with the manufacturer's plate certification and were well within the ASTM specifications. The carbon equivalency number (CEN) was calculated according to [24]. The individual measurements made by OSU to obtain the average composition values are located in [7].

Base Metal Microstructure

The microstructure of the HSLA-80 base metal is shown in the light optical micrograph of Fig. 1. The microstructure is entirely quasipolygonal ferrite. As the base metal was subjected to a precipitation aging heat treatment by the manufacturer, the presence of ε-Cu precipitates is presumed, but they could not be resolved via LOM. The average Vickers microhardness of the base metal was 246 ± 8.2 HV_{200}.

Observing the HSLA-80 base metal in both the longitudinal and transverse planes revealed irregular grains with no significant evidence of rolling texture. The grain size was measured using the "intercept method" detailed in ASTM E1382 [25]. Using this technique, a circle is drawn at random locations within a micrograph, and the number of times a grain boundary intercepts that circle is used to calculate the average grain size. Using a circle instead of a line ensured that rolling texture that may have been present would not bias results. Measurements were taken three times on a sample of base metal with the average ASTM grain size calculated to be $G = 13.2$.

Heat-affected Zone Phase Transformation Analysis

Dilation Curve Analysis Method

Figure 2 shows a representative on-heating portion of a Gleeble-generated dilatometry curve. The black curve (left axis) represents the change in sample diameter with temperature, and nonlinearity in the curve is indicative of a phase transformation's occurrence. Nonlinearity is shown in the red derivative curve (right axis). Linear extrapolations of the black curve are shown by the blue lines. In this case, the transformation of interest is that of the HSLA-80 base metal microstructure to austenite.

Two methods for extracting start and finish temperatures for phase transformations from Gleeble dilatometry data are commonly used. The first method involves superimposing a straight line of matching slope along the low-temperature portion of the dilation curve and extrapolating it past the onset of transformation. The point at which the experimental data begins to deviate from the straight line is then taken as

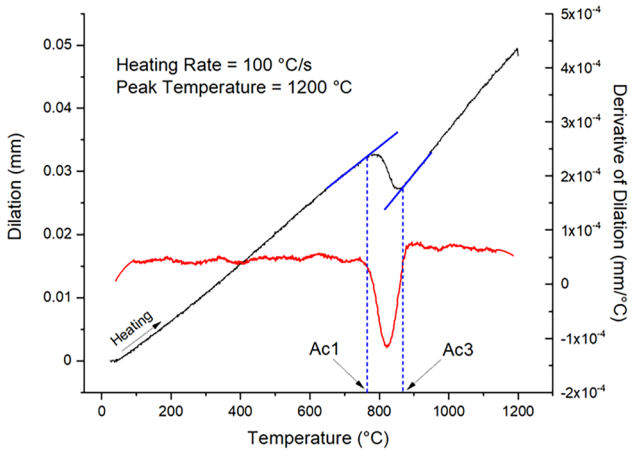

Fig. 2 Representative on-heating dilatometry curve for HSLA-80 steel, showing the linear extrapolation and derivative curve methods for evaluating the ferrite to austenite reaction. Black curve, left axis: dilation data. Red curve, right axis: derivative of dilation data. Blue lines: extrapolation lines for determining transformation start (A_{c1}) and finish (A_{c3}) temperatures

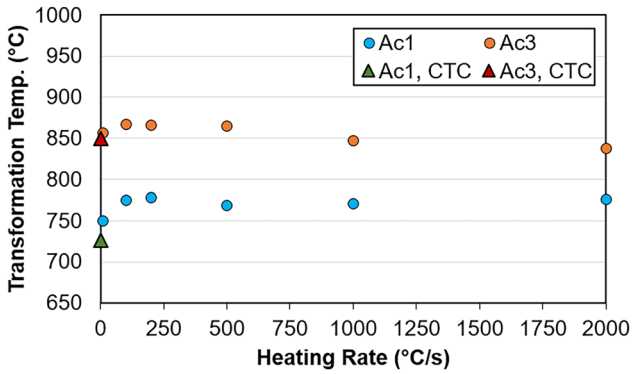

Fig. 3 Variation in austenite transformation start and finish temperatures with heating rate for HSLA-80 material. CTC data from [23]

the transformation start temperature. The same technique is then used to find the transformation finish temperature, with the straight line being extrapolated backward from the high-temperature portion of the curve after the transformation. The second method involves calculating and plotting the derivative of the dilation curve. Then the points at which the derivative begins to deviate from a constant value are taken as the transformation start and finish temperatures. Both methods for determining phase transformation temperatures are inherently somewhat subjective, and both also have advantages and disadvantages. The linear extrapolation method is faster and easier to interpret but is difficult to use when multiple transformations occur. The derivative method is more quantitative and can more easily distinguish multiple transformations but can be difficult to interpret when the dilation data are noisy. For this work, the linear extrapolation method was chosen as the primary method of data analysis, and the derivative method was used as a complementary technique for distinguishing concurrent phase transformations. Both methods are shown in Fig. 2, where the derivative curve is displayed in red (right axis) and the linear extrapolations are displayed in blue.

Austenite Transformation Temperature Measurement

On-cooling solid-state, phase transformation temperatures and products in steels can vary substantially with peak temperature due to differences in austenite grain size at different peak temperatures [26–29]. Thus, it is expected that each of the investigated HAZ regions would produce slightly different CCT diagrams. The residual stress (and subsequent distortion) that develops during weld cooling is greatly influenced by: (1) the microstructure that forms on cooling and (2) the temperature difference between the end of the on-cooling transformations and the final temperature of the component. Thus, full analysis must include as much HAZ phase transformation behavior as possible in order to provide the most complete and accurate material database for welding simulations.

Figure 3 presents the variation in austenite transformation behavior as a function of heating rate for HSLA-80 base material. As shown, the austenite transformation start temperature (A_{c1}) increases significantly as heating rate increases toward 200 °C/s (360 °F/s). This is a consequence of thermal diffusion during increasingly rapid heating outpacing the mass diffusion required for the transformation to take place. In contrast, the austenite transformation finish temperature (A_{c3}) remains more stable across the experimental heating rate range. Researchers who have investigated similar behavior in other ferrous materials have associated heating rate dependencies of the austenite transformation with those of the controlling diffusion mechanism (*i.e.*, volume carbon diffusion or grain boundary substitutional element diffusion), the ferrite recrystallization process, and/or austenite nucleation and growth rates [30–32]. These data are important for the refinement of welding simulation results because different regions of a weldment and its HAZ are subject to significantly different heating rates during the welding process. Thus, the on-heating transformation behavior must be incorporated in order to accurately predict which areas around the weld will transform to austenite, and will therefore be subject to re-transformation (and associated changes in mechanical properties and residual stresses) during cooling. Data from CTC as part of the Navy ManTech program are included for comparison [23]. The raw data points for Fig. 3 can be found at [7].

Continuous Cooling Transformation Diagrams

On-cooling, solid-state phase transformation temperatures and products in steels can vary substantially with peak temperature due to differences in austenite grain size at different peak temperatures [26–29]. It was therefore expected that each of the investigated HAZ regions would produce slightly different CCT diagrams. The residual stress (and subsequent distortion) that develops during weld cooling is greatly influenced by: (1) the microstructure that forms on cooling and (2) the temperature difference between the end of the on-cooling transformations and the final temperature of the component. Thus, full analysis must include as much HAZ phase transformation behavior as possible in order to provide the most complete and accurate material database for welding simulations.

CCT diagrams, assembled from dilatometry of HSLA-80 thermally cycled to peak temperatures representative of the four selected HAZ regions, are given in Figs. 4, 5, 6, 7. The austenite transformation temperatures described above allowed for use of an ICHAZ simulation temperature of 825 °C (1517 °F) for HSLA-80, which was the same as that used for HSLA-65 [6] but 50 °C (90 °F) lower than the temperature used for DH36 [5]. The A_{c1} and A_{c3} temperatures labeled on the CCT diagrams are averages calculated from the individual A_{c1} and A_{c3} values for all of the CCT specimens. The black curves are the actual specimen cooling curves. The target cooling rates for all specimens except those cooled at 100 and 200 °C/s (180 and 360 °F/s) were maintained through the on-cooling phase transformations. The latent heat released during low-temperature transformation slowed the cooling rates of both the 100 °C/s (180 °F/s) and the 200 °C/s (360 °F/s) tests with peak temperatures of 1150 and 1350 °C (2102 and 2462 °F). As a result the target cooling rate was maintained until the start of the transformation, but was slowed as the transformations occurred for samples cooled at 100 and 200 °C/s (180 and 360 °F/s). The raw data for these figures (and all CCT-related information) is given in [7] as raw Gleeble 3500 data files (.d0#) based on their cooling rates as well as in spreadsheet format for calculated data.

The colored symbols in Figs. 4, 5, 6, 7 correspond to the start and finish temperatures for the various on-cooling phase transformations. Three regimes of on-cooling transformation start temperatures were observed across the cooling rate range assessed in this work. The first, associated with

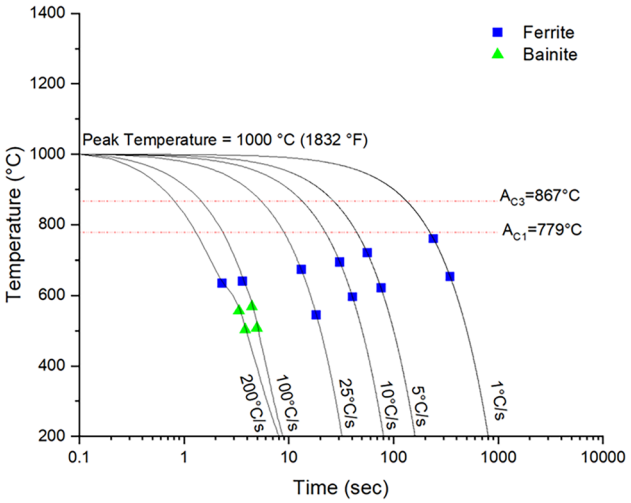

Fig. 5 CCT diagram for HSLA-80 heated to peak temperature of 1000 °C (1832 °F)

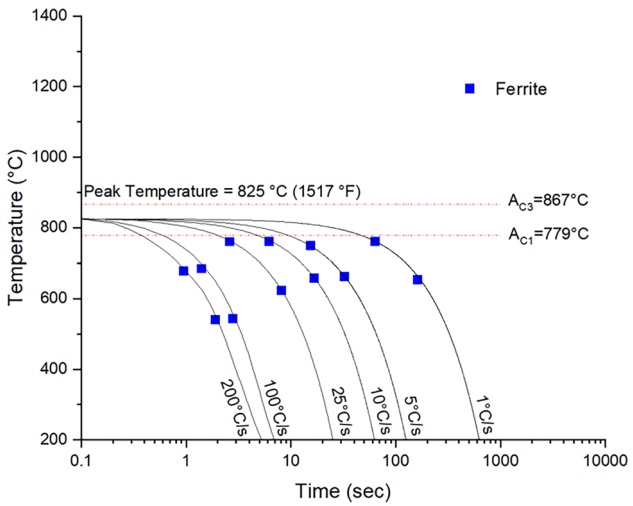

Fig. 4 CCT diagram for HSLA-80 heated to peak temperature of 825 °C (1517 °F)

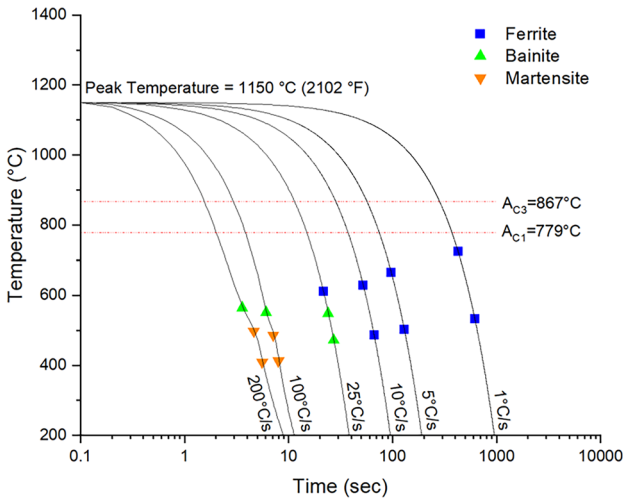

Fig. 6 CCT diagram for HSLA-80 heated to peak temperature of 1150 °C (2102 °F)

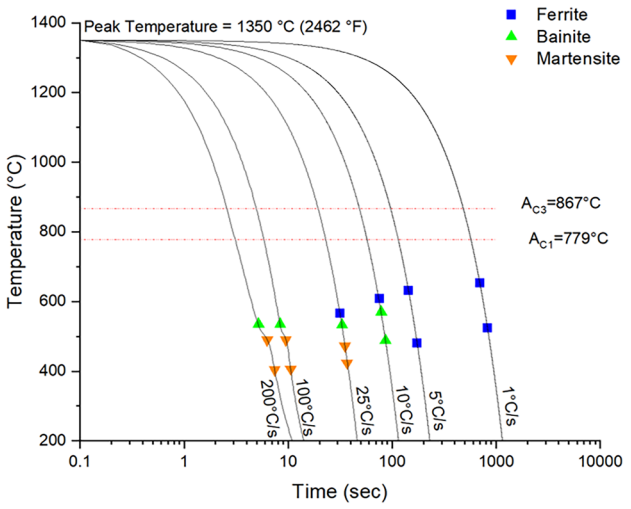

Fig. 7 CCT diagram for HSLA-80 heated to peak temperature of 1350 °C (2462 °F)

ferrite, occurred at high temperatures (567–761 °C [1053 to 1402 °F]) and is denoted in Figs. 4, 5, 6, 7 by blue square symbols. The start of this transformation generally occurred near A_{c1}, though it decreased with increasing peak temperature and increasing cooling rate. The second type of transformation identified is indicated by green triangle symbols, representing the bainite transformation. This transformation started from 38 to 78 °C (100–172 °F) below the start of the higher temperature transformation, with the difference in temperatures dropping as peak temperature increased. The third transformation product identified in the CCT diagrams, indicated as orange triangle symbols, generally started forming at temperatures of 472 to 498 °C (882–928 °F) and was only observed at cooling rates of 25 °C/s (45 °F/s) and higher. The association of this transformation with high peak temperatures indicates that this transformation product is influenced by precipitate dissolution and prior austenite grain (PAG) size. Identification of these transformations is discussed in more detail below, but for interpretation of the diagrams presented in Figs. 4, 5, 6, 7, the blue, red, green, and orange symbols reflect ferrite, bainite, and martensite transformations, respectively.

The effects described above are summarized in an alternate way in Figs. 8, 9, 10. Figure 8 gives the variation in transformation start temperature for the ferrite transformation as a function of peak temperature and cooling rate. As shown, for a given cooling rate, increasing the peak temperature generally suppresses the onset of the transformation, resulting in lower start temperatures. This most likely occurs because PAG size increases with increasing peak temperature, resulting in less grain boundary area and therefore fewer nucleation sites for transformation. For each cooling rate, transformation start temperatures

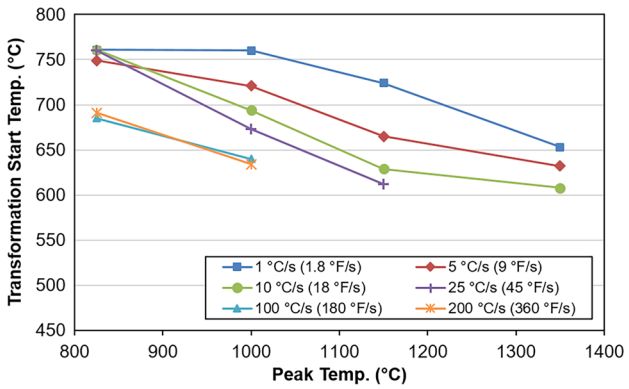

Fig. 8 Variation of start temperature for the ferrite transformation shown in Figs. 4, 5, 6, 7

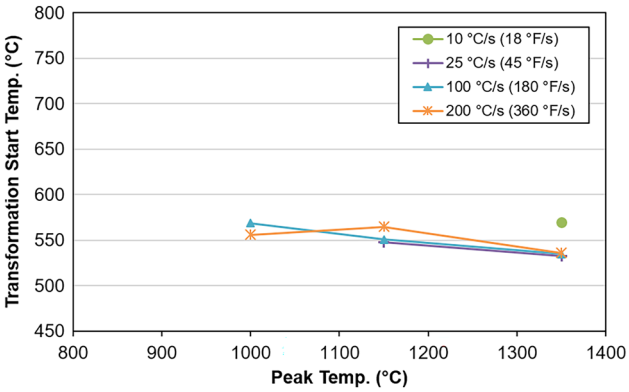

Fig. 9 Variation of start temperature for the bainite transformation shown in Figs. 4, 5, 6, 7

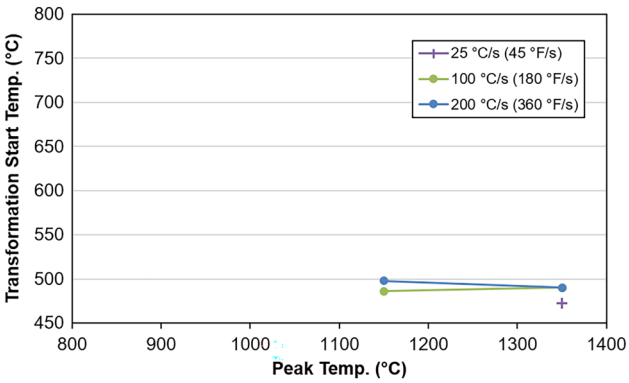

Fig. 10 Variation of start temperature for the martensite transformation shown in Figs. 4, 5, 6, 7

decreased by an average of 48 ± 23 °C (118 ± 73 °F) when compared to the temperature associated with the next highest peak temperature. The onset of transformation is additionally suppressed by undercooling as cooling rate is increased. As a result, transformation start temperature

decreased by an average of 26 ± 23 °C (79 ± 74 °F) for each step in cooling rate tested.

Figure 9 shows that the bainite transformation start temperature did not vary substantially with either peak temperature or cooling rate. All transformation start temperatures fell within the range of 533 to 570 °C (991–1058 °F). It was expected that the bainite transformation temperatures would follow similar trends to those observed for the ferrite transformation, but the small dataset makes trends difficult to confirm.

Martensite was the final transformation product examined, with measured temperatures recorded in Fig. 10. As was the case for bainitic transformation temperatures, the small sample size did not reveal any strong trends associated with peak temperature. Transformations for samples cooled at or above 100 °C/s (180 °F/s) began in the range of 486–498 °C (907–928 °F). The specimen heated to a peak temperature of 1350 °C (2462 °F) and cooled at 25 °C/s (45 °F/s) had a slightly lower transformation start temperature of 472 °C (882 °F). This may be due to the formation of primary ferrite, which was not observed in the more rapidly cooled samples. The low solubility of carbon in ferrite would have enriched the remaining austenite in carbon prior to transformation, thereby stabilizing it to lower temperatures.

In order to confidently establish the identities of the on-cooling phase transformations, LOM was performed on all dilatometry specimens, and select specimens were analyzed via SEM. Individual micrographs collected from the dilatometry specimens are found at [7]. Additionally, the measured microhardness for each specimen is shown in Fig. 11 with raw data found at [7]. For this discussion, the following definitions for the morphology of microstructural constituents are adopted [33–37]. However, the authors recognize that, particularly for bainite, there are alternative and more detailed definitions available in the literature and readers are recommended to investigate further as needed [15–17, 34, 38]. The typical definitions for crystal structure and composition of the constituents are assumed.

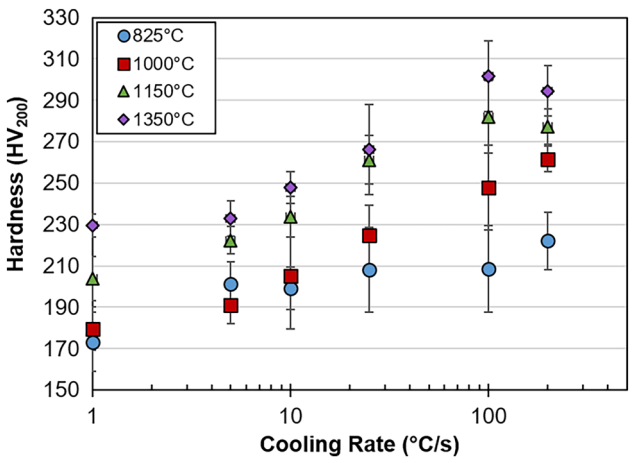

Fig. 11 Measured Vickers microhardness for HSLA-80 dilatometry specimens as a function of peak temperature and cooling rate. Error bars are one standard deviation. Values are the average of 10 indents

Primary ferrite (*FP*)—Carbide-free grain boundary or intragranular allotriomorphic or idiomorphic ferrite, encompassing polygonal (straight grain boundaries) and quasipolygonal (irregular grain boundaries) morphologies

Acicular ferrite (*AF*)—Fine, interlocking structure formed by impingement of multiple Widmanstätten plates growing from intragranular inclusions

Martensite-austenite constituent (*M/A*)—Structure represented by a combination of martensite and residual austenite

Bainite (*B*)—General term for fine aggregates of ferrite laths or plates and cementite particles

Lath martensite (*ML*)—Martensite laths with highly dislocated substructure which are grouped into larger packets

The authors note that for the remainder of this section the labeling of the micro-constituents in Figs. 12, 13, 14, 15, 16, 17 is difficult and in some cases somewhat speculative, based on the limitations of the resolution provided by the metallography and optical microscopy techniques employed, even when considering the correlations between the SEM results and these optical micrographs. Representative micrographs of all CCT specimens heated to 825 °C (1517 °F) are shown in Figs. 12, 13. This peak temperature falls between A_{c1} and A_{c3} (779 and 867 °C [1434 and 1593 °F], respectively) in order to achieve partial transformation to austenite prior to cooling. This partial transformation is expected to occur via austenite nucleation at the triple points and grain boundaries as the ferrite solvus temperature is exceeded [35].

Slowly cooled samples did not retain microstructures from the original base material. The samples subjected to 1, 5, 10, and 25 °C/s (1.8, 9, 18, and 45 °F/s) cooling rates (shown in Fig. 12a–d) all exhibited a mixture of primary ferrite with quasipolygonal morphology and M/A constituent. The proportions of martensite and austenite in the M/A constituents could not be determined through optical or electron microscopy. Additionally, ε-Cu precipitates in HSLA-80 have been reported to be less than 5 nm (2×10^{-7}-in.) in size, so evaluating the impact of HAZ thermal cycling on these precipitates was not within the scope of microscopy in this work. Any volumetric change associated with ε-Cu dissolution was not large enough to identify on dilation curves. For HSLA-80, the dissolution of second phases including ε-Cu was determined in CTC investigations to finish at 880 °C (1616 °F) at slow heating rates [23]. Further, a study by Bhagat et al. indicated that under isothermal aging conditions, dissolution of copper precipitates in an HSLA

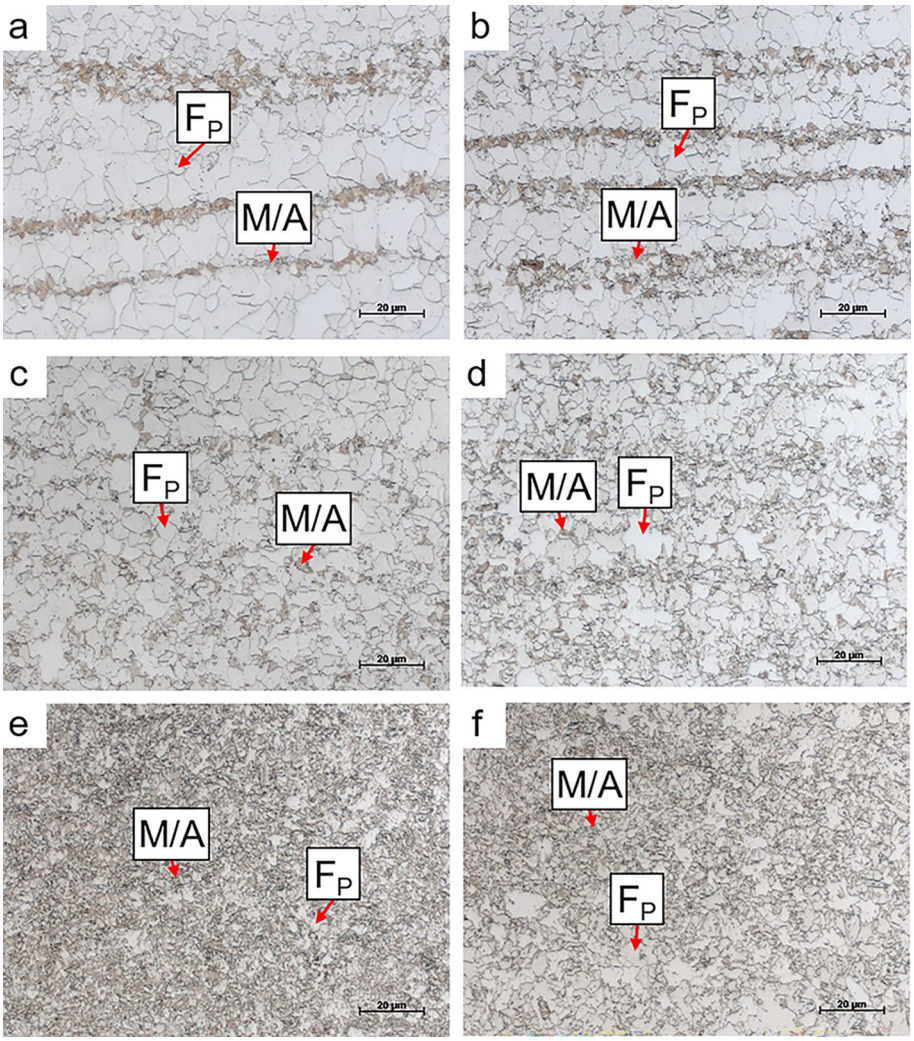

Fig. 12 Representative microstructures from HSLA-80 dilatometry specimens heated to a peak temperature of 825 °C (1517 °F) and continuously cooled at various rates. **a–f** 1, 5, 10, 25, 100, and 200 °C/s (1.8, 9, 18, 45, 180, and 360 °F/s)

steel sample began at 650 and 700 °C (1202 and 1292 °F) after being held for 20 and 4 min, respectively, as evidenced by an increase in experimentally measured resistivity [39]. The sample studied by Bhagat et al. had a composition that was similar to that of HSLA-80, but the Ni content of 3.39 wt.% fell well outside the range of 0.70–1.00 wt.% specified by Tech Pub 300 [4]. Mn, Cr, Mo, and Cu were also slightly higher than the respective allowable ranges for HSLA-80. Thermo-Calc 2020b and the TCFE9 databases were used in this study to calculate an ε-Cu dissolution temperature of approximately 730 °C (1346 °F) for the HSLA-80 composition reported in Table 3 [40]. It is therefore unclear whether ε-Cu precipitates persisted at the 825 °C (1517 °F) ICHAZ peak temperature, but complete dissolution was expected for all higher peak temperature samples. *SYSWELD* does not explicitly account for M/A constituent or precipitates of any kind, so phase fractions of these specimens were reported to be entirely ferrite, as shown in Table 4. The authors speculate this is due to limitations in the number of "phases" available for a user to input into the *SYSWELD* software code, which is set at six. As this set of six "phases" must include both the liquid phase and a fictive phase to represent weld material prior to melting, the remaining four solid phases limits the software's ability to handle all of the different micro-constituents associated with HSLA-type steels.

The average size of the M/A constituent appeared to decrease as cooling rate increased. Evidence of M/A constituent banding was present in the 1 °C/s (1.8 °F/s) and, to a lesser degree, in the 5 °C/s (9 °F/s) specimens. M/A constituent formation requires local carbon enrichment. Austenite has a significantly higher solubility for carbon than ferrite does, so partial transformation of the ferritic base material into austenite would have encouraged diffusion of carbon from ferritic regions to austenitic ones. Further, banding of alloying elements or impurities is a common phenomenon in rolled plate. A calculation performed using Thermo-Calc 2020b and the TCFE9 thermodynamic database [40] predicted that the chemical potential of carbon would be lower in areas where remnant macrosegregation of substitutional elements was present, further driving diffusion toward those

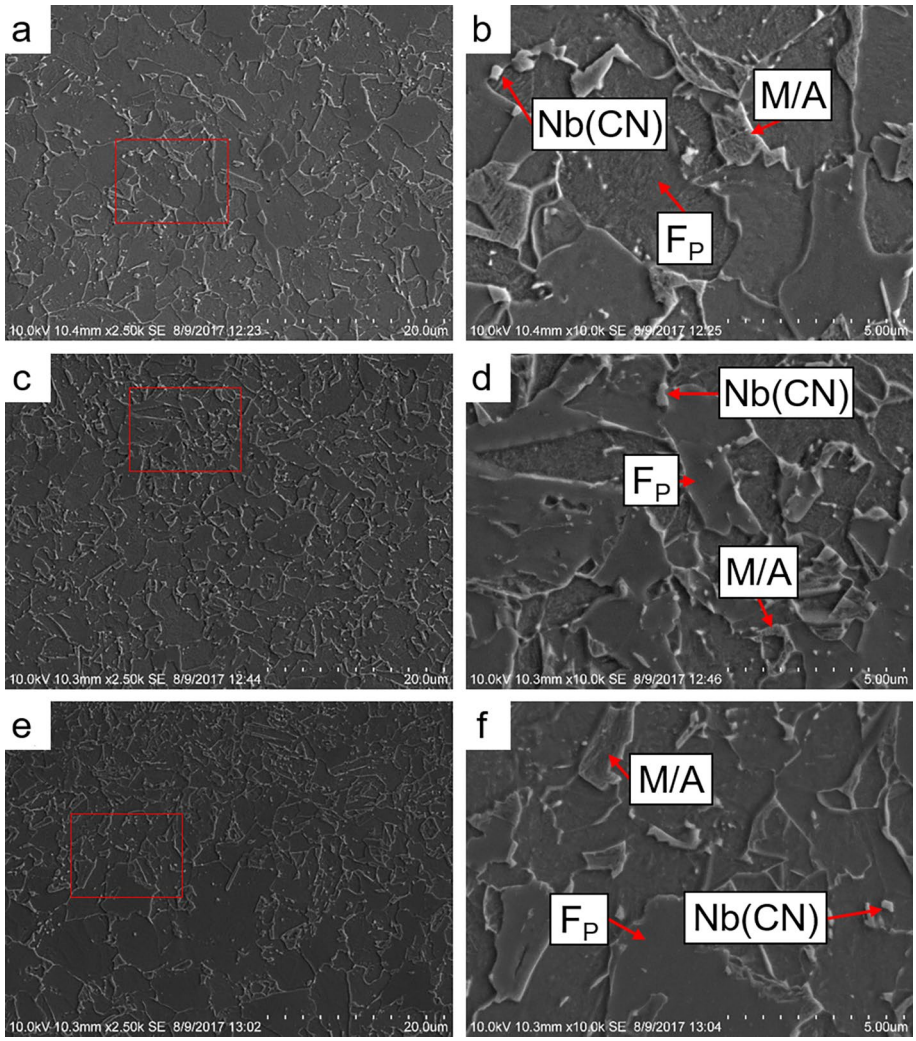

Fig. 13 SEM images of the microstructure of a HSLA-80 dilatometry specimen heated to a peak temperature of 825 °C (1517 °F) and rapidly cooled. Red boxes overlaid on images in the left column demarcate the location of the higher magnification images in the right column. **a**–**f** 25, 25, 100, 100, 200, 200 °C/s (45, 45, 180, 180, 360, 360 °F/s). Constituents identified as carbonitrides (CN) were not compositionally characterized but are presumed based on the known metallurgy and composition of the alloy

areas. This effect was predicted for every intentional alloying addition with the exception of Si and Mo, which had the opposite effect.

Diffusion of carbon toward banded regions of alloying elements explains the presence of M/A constituent in bands upon cooling. The absence of such banding in specimens heated to higher peak temperatures is expected, as these samples spent more time in high-temperature regimes. These temperatures are associated with higher mobility of alloying elements, and with sufficient time they are able to thoroughly diffuse and create a homogeneous distribution rather than one with locally enriched regions. Increased cooling rates were also associated with an increasing number of small precipitates. Microhardness increased slightly from 173 to 208 HV_{200} for samples cooled from 1 to 25 °C/s (1.8–45 °F/s). This is likely due to two simultaneous phenomena: first, strengthening from the increased number of precipitates; and second, a Hall–Petch effect from the decreased ferrite grain size in recrystallized areas, as is qualitatively apparent in Fig. 12a–d. Only one transformation was detected in the on-cooling dilation data for each of these samples. Transformation start temperatures remained stable at approximately 761 °C (1402 °F) across this range of cooling rates, with the exception of the sample cooled at 5 °C/s (9 °F/s), with a measured transformation start temperature of 749 °C (1380 °F). Transformation finish temperatures fell from 653 to 624 °C (1207 to 1155 °F), with a slight increase to 663 °C (1225 °F) for the sample cooled at 5 °C/s (9 °F/s). As was seen during previous investigations of DH36 [5] and HSLA-65 [6] steels, there was no discernible transformation temperature for M/A constituent; rather, the temperatures described were associated with transformation from austenite to ferrite.

Samples cooled at 100 and 200 °C/s (180 and 360 °F/s) were composed of fine quasipolygonal ferrite, M/A constituent, and precipitates of approximately 0.1–0.2 μm ($3.9–7.9\times10^{-6}$-in.) in diameter, as shown in Fig. 13. Identification of precipitation composition was outside the scope of the present investigation, as such attributes are not explicitly accounted for in finite element welding process models. It is

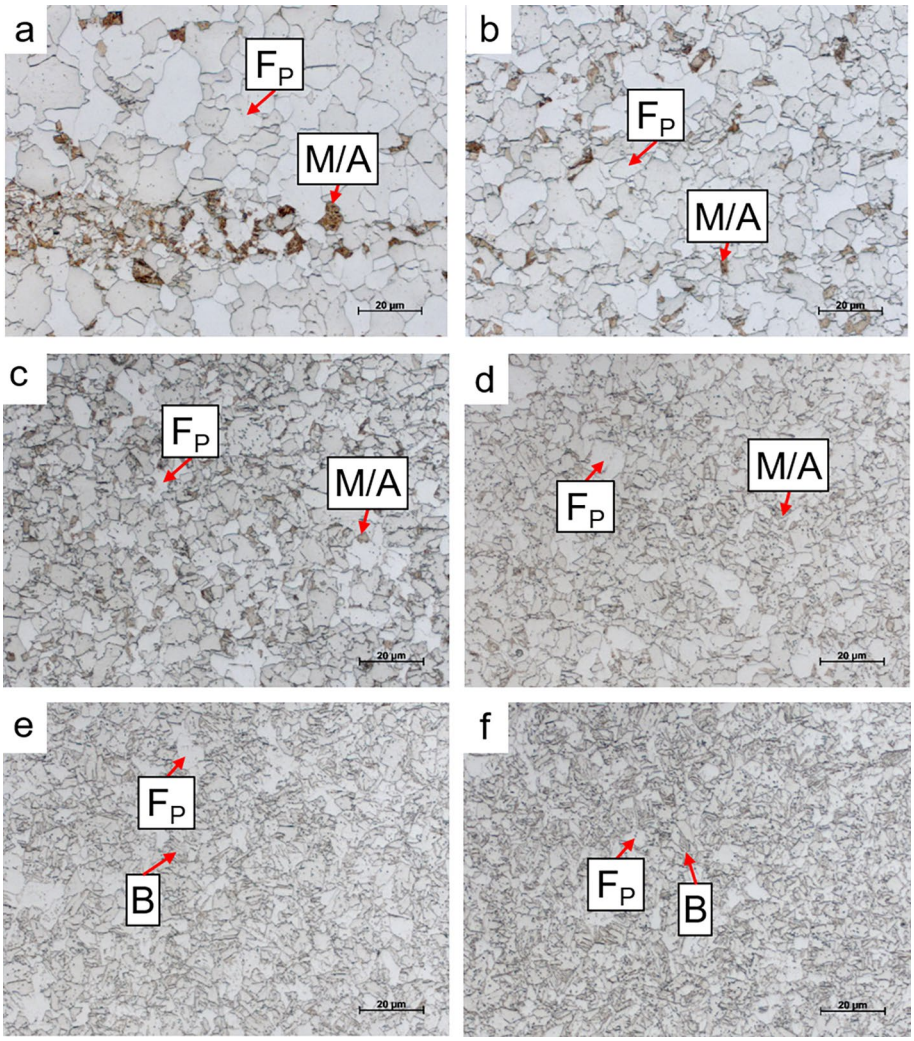

Fig. 14 Representative microstructures from HSLA-80 dilatometry specimens heated to a peak temperature of 1000 °C (1832 °F) and continuously cooled at various rates. **a–f** 1, 5, 10, 25, 100, and 200 °C/s (1.8, 9, 18, 45, 180, and 360 °F/s)

assumed that these include niobium-carbonitride [Nb(CN)] precipitates, as these are intentionally induced in HSLA-80 base material for precipitation strengthening but would not have dissolved into solid solution at such a low peak temperature [27]. It should be noted that the labeled Nb(CN) precipitates can appear to be larger than might be expected due to etching and imaging effects within the SEM. Additionally, it is also assumed that other, finer Nb(CN) could well have been present but are not resolved. Transformation start temperatures of 685 and 691 °C (1265 and 1276 °F) were slightly lower than those measured for more slowly cooled specimens, with finish temperatures of 543 and 540 °C (1009 and 1004 °F), respectively.

It is acknowledged that the phase fraction of the two rapidly cooled specimens qualitatively appears to have a high proportion of M/A constituent. This dark-etched constituent bears a resemblance to martensite and, as the name implies, may be partially composed of martensite. Despite this, the high transformation temperatures, the low microhardness values of 209 and 220 HV_{200}, and the absence of martensite in rapidly cooled samples heated to the next highest peak temperature of 1000 °C (1832 °F) support the identification of M/A constituent. As discussed previously, for the purposes of *SYSWELD* simulations this is not considered to be a distinct phase and is reported as 100% ferrite in Table 4. However, due to the sheer quantity in these samples, other investigations may benefit from closer examination and characterization of this constituent.

Optical micrographs of HSLA-80 specimens heated to 1000 °C (1832 °F) are shown in Fig. 14 with measured phase fractions in Table 5. These samples were intended to reproduce FGHAZ microstructures and thus were fully austenitized prior to cooling. The microstructures observed in samples cooled from 1–25 °C/s (1.8–45 °F/s) were the same as those formed in the corresponding ICHAZ samples: primary ferrite and M/A constituent. The higher peak temperature produced a slightly larger grain size in the sample cooled at 1 °C/s (1.8 °F/s) due to the increased time available for grain growth above A_{c3}. The M/A constituent banding that was observed in slowly cooled ICHAZ

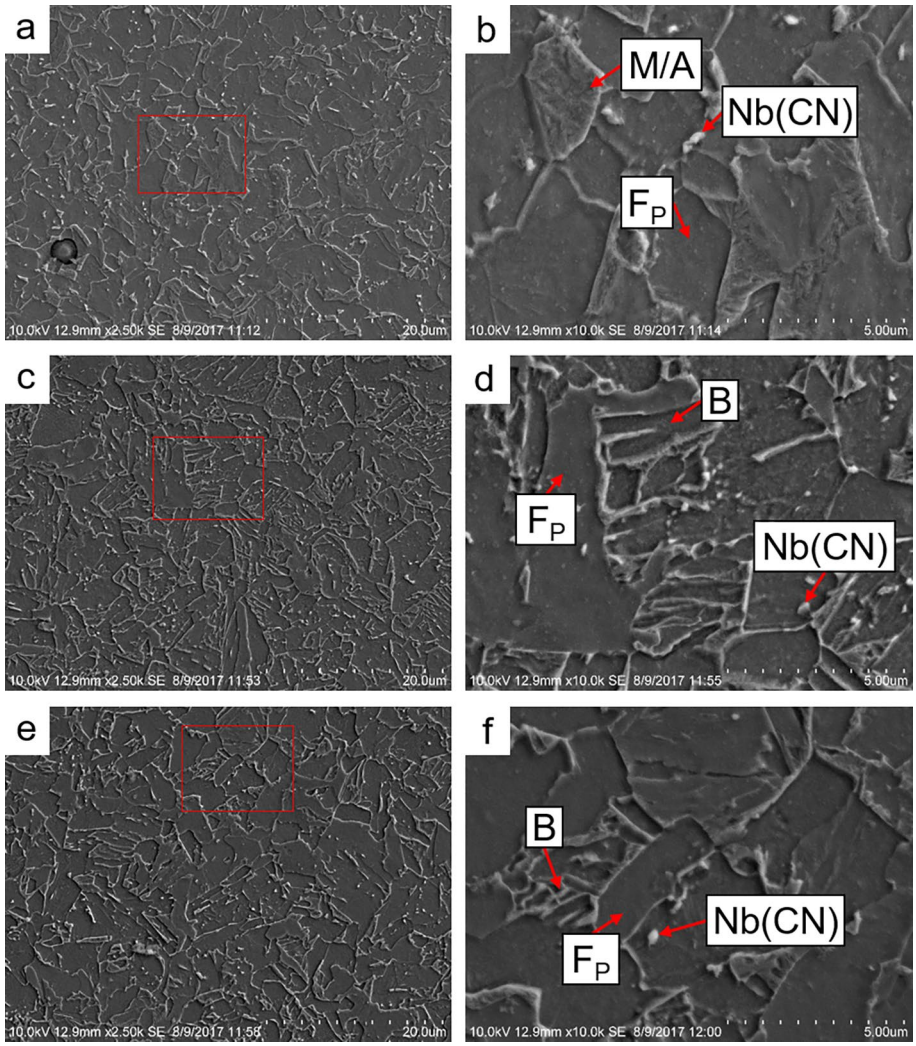

Fig. 15 SEM images of the microstructure of a HSLA-80 dilatometry specimen heated to a peak temperature of 1000 °C (1832 °F) and rapidly cooled. Red boxes overlaid on images in the left column demarcate the location of the higher magnification images in the right column. **a**–**f** 25, 25, 100, 100, 200, 200 °C/s (45, 45, 180, 180, 360, 360 °F/s). Constituents identified as carbonitrides (CN) were not compositionally characterized but are presumed based on the known metallurgy and composition of the alloy

samples was absent in samples heated to 1000 °C (1832 °F), likely because increased time at high temperature allowed diffusion of alloying elements and partial homogenization of the austenitic solid solution. Microhardness values mirrored those of the lower peak temperature at cooling rates less than 25 °C/s (45 °F/s), falling between 180 and 205 HV_{200}. Microhardness for the 25 °C/s (45 °F/s) cooled sample was 225 ± 15 HV_{200}, which is 17 HV_{200} lower than the corresponding ICHAZ sample as a result of the finer grain structure. Transformation start temperatures for these four cooling rates fell from 760 to 673 °C (1400 to 1243 °F) as cooling rate increased.

Samples cooled at 100 and 200 °C/s (180 and 360 °F/s) were predominantly composed of fine quasipolygonal ferrite. Undercooling caused a drop in transformation temperatures to 640 and 634 °C (1183 and 1243 °F), respectively, driving a morphological shift from the relatively equiaxed ferrite found in more slowly cooled samples. A substantial increase in microhardness was associated with this change in morphology, rising to 248 ± 21 and 262 ± 6 HV_{200} for the 100 and 200 °C/s (180 and 360 °F/s), respectively. In addition to ferrite, there appeared to be small packets of bainite. These are visible in Fig. 15 as small packets of aligned ferrite laths.

The visual difference between ferrite and bainite can be subtle, particularly when small prior austenite grain sizes do not allow for the growth of long, high aspect ratio laths. Various constitutive equations for predicting the start temperatures for bainite and martensite transformations based on alloy chemistry are available in the literature [41, 42]. Such models are generally oversimplifications and often are only accurate for alloys similar to those used to create them, but they can act as a guide for reasonable temperatures at which to expect formation of intermediate and low-temperature phases. As such, the models developed by Capdevilla et al. [43] and Kirkaldy [44] were applied to the averaged HSLA-80 composition given in Table 3:

$$M_s = 491.05 - 302.6w_C - 30.6w_{Mn} - 16.6w_{Ni} - 8.9w_{Cr} + 2.4w_{Mo} - 11.3w_{Cu} + 8.58w_{Co} + 7.4w_W - 14.5w_{Si} \quad (5)$$

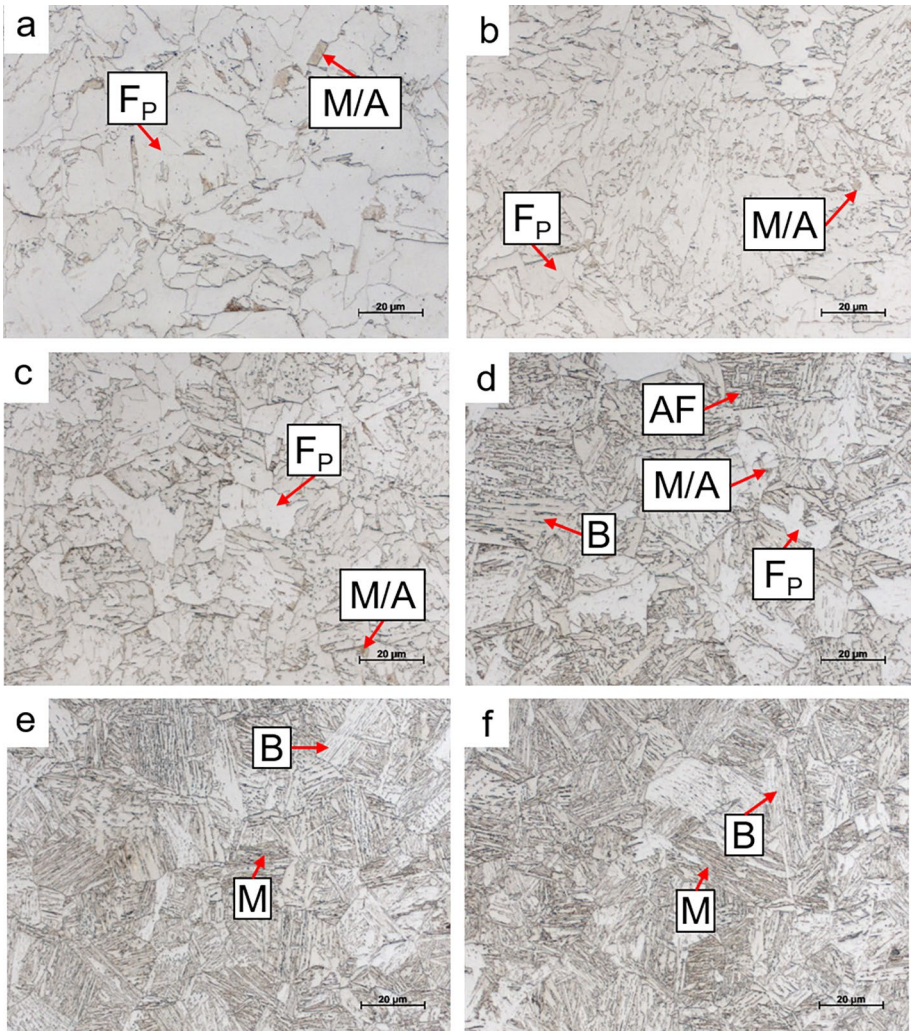

Fig. 16 Representative microstructures from HSLA-80 dilatometry specimens heated to a peak temperature of 1150 °C (2102 °F) and continuously cooled at various rates. **a–f** 1, 5, 10, 25, 100, and 200 °C/s (1.8, 9, 18, 45, 180, and 360 °F/s)

$$B_s = 656 - 57.7w_C - 75w_{Si} - 35w_{Mn} - 15.3w_{Ni} - 32w_{Cr} - 41.2w_{Mo} \quad (6)$$

where M_s = martensite start temperature (°C), B_s = bainite start temperature (°C), w_i = concentration of element i (wt.%).

From Eqs. 5 and 6, the M_s and B_s temperatures for HSLA-80 are predicted to be 425 °C (798 °F) and 571 °C (1060 °F), respectively. The temperature ranges observed in rapidly cooled samples heated to 1000 °C (1832 °F) are 640–507 °C (1184–945 °F) and 634–503 °C (1173–937 °F), encompassing the predicted bainite transformation temperature. This and the relatively high microhardness values of 248 ± 20 and 262 ± 6 HV_{200} both support identification of the secondary phase as bainite. Primary ferrite and bainite are both shown in the micrographs in Fig. 15c–f. Featureless grains with no internal texture aside from the occasional carbonitride were identified as primary ferrite. Grains that were populated with aligned, high aspect ratio laths were identified as bainite.

Representative microstructures of samples heated to 1150 °C (2102 °F) are shown in Fig. 16 with measured phase fractions reported in Table 6. Samples cooled at rates from 1–10 °C/s (1.8–18 °F/s) resulted in mixtures of polygonal and quasipolygonal ferrite interspersed with small islands of M/A constituent. These are the same phases associated with slow cooling for the two lower peak temperatures, but the 1150 °C (2102 °F) temperature was sufficient for grain growth. Increasing cooling rate to 25 °C/s (45 °F/s) introduced acicular ferrite and bainite to the quasipolygonal ferrite and M/A constituent observed in more slowly cooled samples. Transformation start and finish temperatures both fell as cooling rate increased, dropping from 665 to 612 °C (1129 to 1134 °F) and from 503 to 472 °C (937 to 882 °F), respectively. Similarly, microhardness increased from 222 ± 7 to 261 ± 12 HV_{200} with the shift from the softer phases formed during slow cooling.

Cooling rates of 100 and 200 °C/s (180 and 360 °F/s) were too rapid for formation of ferrite. Instead, microstructures consisted of a mixture of bainite and martensite,

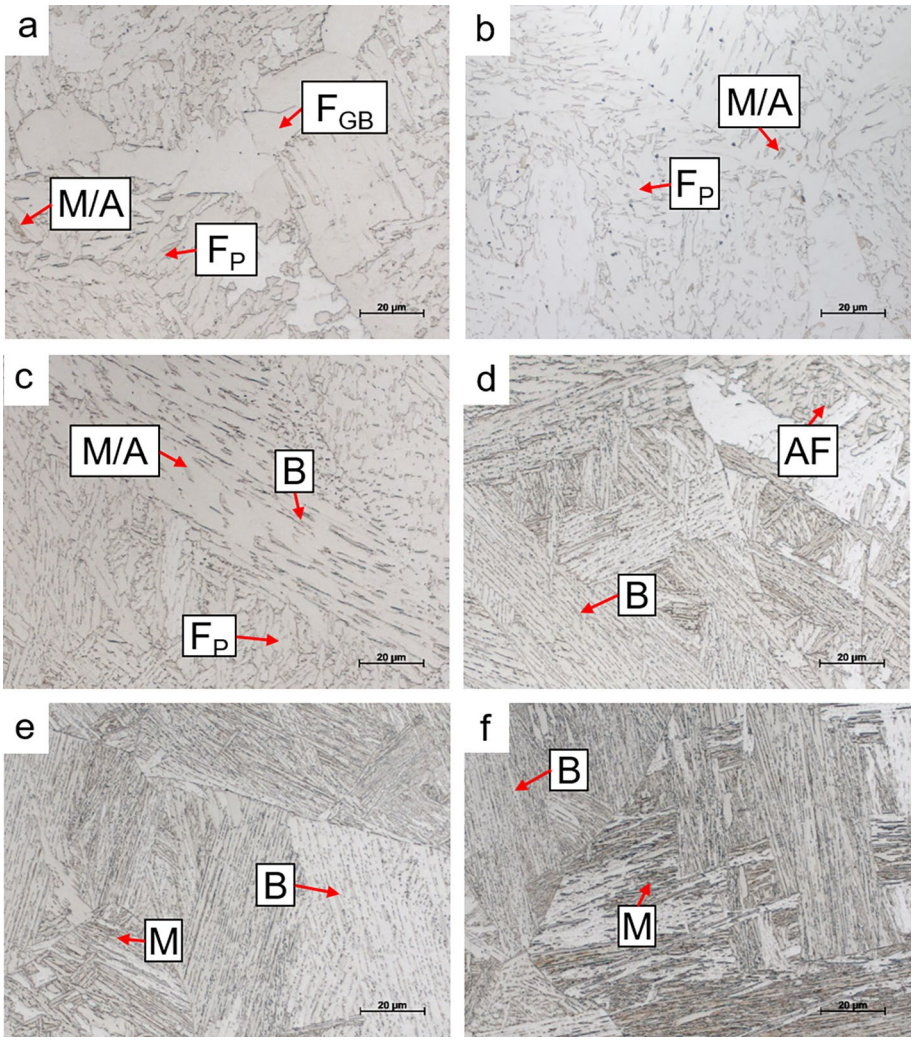

Fig. 17 Representative microstructures from HSLA-80 dilatometry specimens heated to a peak temperature of 1350 °C (2462 °F) and continuously cooled at various rates. **a–f** 1, 5, 10, 25, 100, and 200 °C/s (1.8, 9, 18, 45, 180, and 360 °F/s)

Table 4 Measured phase fraction of HSLA-80 CCT specimens thermally cycled to a peak temperature of 825 °C (1517 °F)

Cooling Rate		Peak Temperature = 825 °C (1517 °F)		
°C/s	°F/s	F + M/A	B	M
1	1.8	1.0	0	0
5	9	1.0	0	0
10	18	1.0	0	0
25	45	1.0	0	0
100	180	1.0	0	0
200	360	1.0	0	0

Table 5 Measured phase fraction of HSLA-80 CCT specimens thermally cycled to a peak temperature of 1000 °C (1832 °F)

Cooling Rate		Peak Temperature = 1000 °C (1832 °F)		
°C/s	°F/s	F + M/A	B	M
1	1.8	1.0	0	0
5	9	1.0	0	0
10	18	1.0	0	0
25	45	1.0	0	0
100	180	0.98	0.02	0
200	360	0.94	0.06	0

as shown in Fig. 16e–f. The differentiation between the two phases was based on the relative grayscale color of the different areas (*i.e.*, lighter vs. darker) as well as morphological differences in the lath structure. The bainite start temperature was measured to be 551 and 565 °C (1024 and 1049 °F) for the 100 and 200 °C/s (180 and 360 °F/s) samples, respectively. While the martensite start temperature was difficult to discern from the dilation data, the finish temperatures were 412 and 409 °C (774 and 768 °F), respectively. As expected, microhardness was higher than all previously discussed specimens at 282 ± 18 and 277 ± 9 HV_{200}.

Table 6 Measured phase fraction of HSLA-80 CCT specimens thermally cycled to a peak temperature of 1150 °C (2102 °F)

Cooling Rate		Peak Temperature = 1150 °C (2102 °F)		
°C/s	°F/s	F + M/A	B	M
1	1.8	1.0	0	0
5	9	1.0	0	0
10	18	1.0	0	0
25	45	0.85	0.15	0
100	180	0	0.76	0.24
200	360	0	0.62	0.38

Table 7 Measured phase fraction of HSLA-80 CCT specimens thermally cycled to a peak temperature of 1350 °C (2462 °F)

Cooling Rate		Peak Temperature = 1350 °C (2462 °F)		
°C/s	°F/s	F + M/A	B	M
1	1.8	1.0	0	0
5	9	1.0	0	0
10	18	0.80	0.20	0
25	45	0.04	0.96	0
100	180	0	0.43	0.57
200	360	0	0.62	0.38

The last set of samples were heated to 1350 °C (2462 °F) in order to simulate the CGHAZ. Representative optical micrographs are presented in Fig. 17 and corresponding phase fractions are reported in Table 7. As previously stated, the differentiation between the various phases was based on the relative grayscale color of the different areas (*i.e.*, lighter vs. darker) as well as morphological differences, in particular: aspect ratio, orientation with respect to adjacent features (*e.g.,* laths and prior austenite grain boundaries), and the presence or absence of intragranular texture. HSLA-80 derives strength from both ε-Cu and Nb(CN) precipitates, which pin austenite grain boundaries and maintain a fine grain structure [27]. At temperatures above equilibrium dissolution temperature, precipitates dissolve into solid solution and allow for unhindered austenite grain growth. This is demonstrated in the specimen cooled at 1 °C/s (1.8 °F/s), which presented significantly larger ferrite grains than those formed at lower peak temperatures. As noted above, Bhagat et al. indicated that under isothermal aging conditions, dissolution of copper precipitates occurred at 650 °C (1202 °F) [39], and calculations in this study predicted an ε-Cu dissolution temperature near 730 °C. From this, it can be assumed that dissolution of ε-Cu precipitates was complete for each peak temperature investigated, and thus does not explain the increased grain size only observed at the 1350 °C (2462 °F) peak temperature. Shome and Mohanty [27] calculated Nb(CN) precipitate dissolution by applying the invariant size model to a precipitate size of 0.02 μm (7.9×10^{-7}-in.). For heat inputs of 10 and 40 kJ/cm (25.4 and 101.6 kJ/in), dissolution temperature was predicted to be 1245 and 1200 °C (2273 and 2192 °F), respectively. No attempt was made to identify precipitate dissolution temperatures in the present study, but the significant increase in grain size between peak temperatures of 1150 and 1350 °C (2102 and 2462 °F) is consistent with dissolution temperatures predicted by Shome and Mohanty [27]. High-temperature phase dissolution was also predicted using Thermo-Calc 2020b and the TCFE9 database [40]. Under the equilibrium conditions assumed in the calculations, dissolution of Nb(CN) was predicted to occur at approximately 1115 °C (2039 °F). Though precipitate size was not quantified during this study, it is likely that Gleeble test conditions more closely mirrored those examined in the study by Shome and Mohanty, with precipitate dissolution temperatures approaching temperatures at or above 1200 °C (2192 °F) [27]. This is further suggested by the lack of significant grain growth observed in samples heated to 1150 °C (2102 °F). The minute volumetric change associated with precipitate evolution and dissolution meant that neither could be detected in dilatometry curves to confirm this conclusion.

As shown in Fig. 17a, the sample cooled at 1 °C/s consisted of primary ferrite decorating large prior austenite grain boundaries along with quasipolygonal ferrite that had formed intragranularly. The association of F_{GB} with prior austenite grains is more readily apparent at lower magnifications due to the large prior austenite grain size. Small islands of dark-etched M/A constituent were also present, dispersed among the quasipolygonal ferrite. The large prior austenite grain size corresponds with a smaller total length of grain boundary. Without these energetically favorable ferrite nucleation points, ferrite formation was suppressed below transformation temperatures observed in previous specimens—transformation start and finish temperatures were 653 and 524 °C (1207 and 975 °F), respectively. The increased proportion of quasipolygonal ferrite (compared to polygonal ferrite) is associated with a higher hardness than seen in slow-cooled samples with lower peak temperatures, measuring 230 ± 6 HV_{200}. Grain boundary ferrite was eliminated from the sample cooled at 5 °C/s (9 °F/s), leaving a mixture of quasipolygonal ferrite and M/A constituent. Bainite was introduced to that mixture in the sample cooled at 10 °C/s (18 °F/s), taking the form of high aspect ratio ferrite grains with an aligned second, dark-etched phase between laths. The low alloy content was responsible for the discontinuous nature of that secondary phase. The large prior austenite grain size discussed previously discouraged formation of polygonal ferrite, allowing formation of bainite at lower cooling rates than observed for lower peak

temperatures. Transformation start temperatures fell from 632 to 603 °C (1170 to 1117 °F) as cooling rate increased, though transformation finish temperatures remained approximately steady at 494 and 493 °C (921 and 919 °F). Microhardness increased 233 ± 9 to 248 ± 8 HV_{200} with increased cooling rate, indicative of the introduction of bainite.

Increasing cooling rate to 25 °C/s (45 °F/s) produced a microstructure that was primarily bainite with a small amount of acicular ferrite, as shown in Fig. 17d. Acicular ferrite was identified as light-etched grains with high aspect ratio that were not aligned in the same manner as bainite. Instead, acicular ferrite grains likely nucleated from Nb(CN) and grew in orientations corresponding to those precipitates rather than the parent austenite grain. These competing grains impinged upon one another, limiting growth and manifesting at room temperature as fine ferrite grains with higher aspect ratio than those associated with polygonal ferrite. Acicular ferrite is associated with a high degree of undercooling and thus with high cooling rates. In samples cooled at the same rate but heated to a lower peak temperature, the extensive network of prior austenite grain boundaries associated with the smaller grain size likely acted as more favorable nucleation sites for ferrite, allowing transformation of polygonal or quasipolygonal ferrite before reaching low temperatures where nucleation of acicular ferrite was energetically favorable. The temperature associated with initial transformation from austenite fell further from that of more slowly cooled samples, measured to be 567 °C (1053 °F) for the sample cooled at 25 °C/s (45 °F/s). This likely corresponded with the bainite transformation, with the proportion of acicular ferrite too small to discern in the dilation curve, though acicular ferrite is also associated with low transformation temperatures. Martensite was not observed in micrographs, though the low transformation finish temperature of 424 °C (795 °F) supports its presence in very small amounts. The large standard deviation of microhardness data is also indicative of the wide range of phases: microhardness was measured to be 266 ± 22 HV_{200}. Further increases in cooling rate to 100 and 200 °C/s (180 and 360 °F/s) resulted in dual phase microstructures of bainite and martensite, with bainite transformation start temperatures of 535 and 536 °C (995 and 997 °F), respectively. The martensite start temperature was difficult to discern, but appeared to be 490 °C (914 °F) for both specimens. This transformation completed at 408 and 404 °C (766 and 759 °F) for the 100 and 200 °C/s (180 and 360 °F/s) samples, respectively. Microhardness values were also quite similar, measuring 302 ± 17 and 295 ± 12 HV_{200}. Optical micrographs of these two specimens are shown in Fig. 17e–f.

It is noted that in several dilation curves, there is a high temperature anomaly which is not associated with the microstructural evolution discussed previously. Under ideal experimental conditions the austenitic portion of the dilation curve would have an approximately linear slope. The dilation curves for samples heated to 1350 °C (2462 °F) each show two distinct portions, with the high-temperature portion appearing to decrease in dilation more rapidly with respect to temperature. This is not the result of a phase transformation; rather, it reflects deformation of the specimen by the small force exerted by the Gleeble jaws. The low strength of the material at such a high temperature was evidenced by the dip in the cooling portion of the CCT curves and was further supported by micrographs showing enlarged austenite grains, which were present due to dissolution of strengthening precipitates and indicated a low strength microstructure in the high-temperature regime. The dilation curve returns to a linear rate of contraction as specimens recover strength at temperatures lower than approximately 1100 °C (2012 °F). The same phenomenon was observed in samples heated to 1150 °C (2102 °F) but the reduced time at high temperatures rendered the effect less pronounced.

The phase transformation information developed here is critically important for ensuring that weld simulation software can draw on thermo-physical and thermo-mechanical property information from the appropriate phases at the appropriate times during calculations. However, as mentioned at the beginning of this section, the identification and quantification of the micro-constituents based on the optical microscopy and SEM results provided is somewhat subjective. Therefore, the quantification of micro-constituents in Tables 4, 5, 6, and 7 should be considered semi-quantitative. Lastly, the results in Figs. 4, 5, 6, 7 highlight the importance of developing multiple HAZ-related CCT diagrams for any other projects seeking to complete similar testing for other alloys.

Weldment Microstructures

Metallographic specimens were removed from both weldments and analyzed in a manner similar to the Gleeble specimens. Discussion of microstructures present correspond to the HAZ of the second pass for each weldment, as the reheating experienced by the first pass confounded the analysis and did not directly correlate with thermal cycles undergone by Gleeble CCT specimens. All raw data for the charts can be found in [7].

The tee joint fusion zone was a mixture of coarse primary ferrite, acicular ferrite, and unidentified carbides. Figure 18 presents representative micrographs from HAZ of the tee joint. Figure 18a shows that the CGHAZ was composed of upper bainite with quasipolygonal primary ferrite. Figure 18b shows that the FGHAZ directly adjacent to the CGHAZ was composed of the same microstructures, with an increased proportion of ferrite. Figure 18c shows that as distance increased from the fusion line, bainite was no longer present in the FGHAZ. Instead, phases present

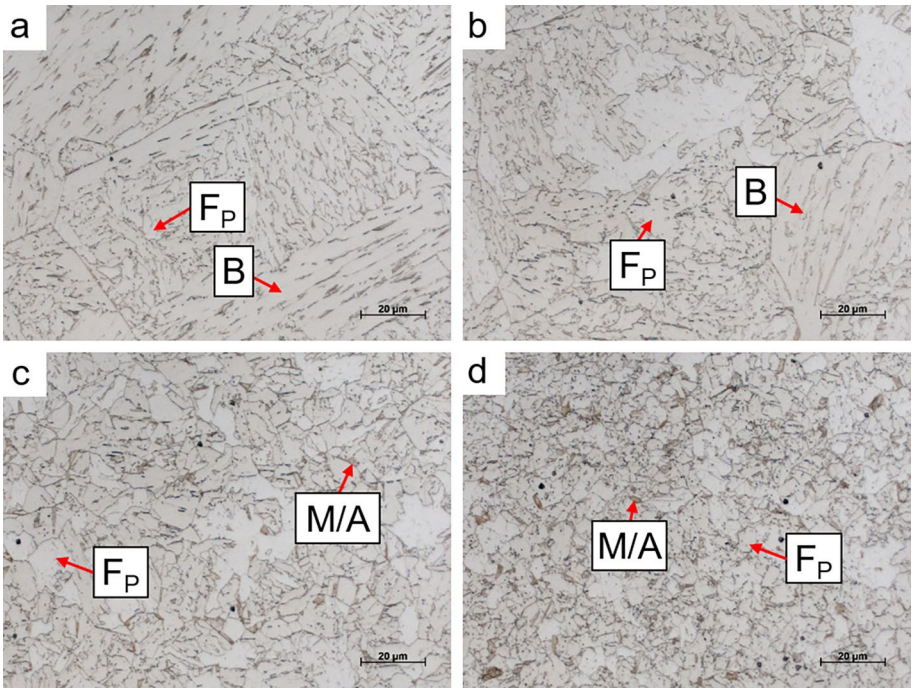

Fig. 18 Representative light optical micrographs of the second pass of the HSLA-80 tee joint showing the **a** CGHAZ, **b** FGHAZ close to the CGHAZ, **c** FGHAZ close to the ICHAZ, and **d** ICHAZ

included quasipolygonal ferrite and islands of M/A constituent. These same phases appeared in the ICHAZ, as shown in Fig. 18d, with a finer grain size. The dilatometry specimen microstructures that most closely correspond with those observed in the fillet weld CGHAZ, FGHAZ, and ICHAZ are those associated with 10 °C/s (18 °F/s) cooling. There is good agreement with the microhardness values of the Gleeble samples cooled at 10 °C/s (18 °F/s), which fell within the range of 199–248 HV_{200}, and those of the weldment HAZ, falling within the range of 165–255 HV_{200}.

The light optical micrographs in Fig. 19 demonstrate placement of microhardness indents within the microstructural gradient of the tee joint's HAZs. Figure 20 shows the averaged measurements from the three linear patterns associated with each weld bead. Microhardness data are presented as distance from the fusion line, though the width of the heat-affected zone varied depending on location within the weldment (*i.e.*, near the surface or the center of the plate) because of the small plate thickness. As such, care should be taken when comparing values taken at the same distance from the fusion line, as they do not necessarily correspond with the same region of the HAZ. Inconsistencies also exist between microhardness values at the same linear distance from the fusion line due to challenges associated with collecting hardness traverses perpendicular to the non-semicircular HAZ boundaries in thin plates. Nevertheless, trends for the HAZ microhardness were consistent for microhardness patterns measured in comparable locations of each bead (*e.g.*, patterns 1 and 2). There was a significant increase of approximately 26 HV_{200} for measurements in the fusion zone and CGHAZ. Microhardness then fell steadily with distance from the fusion line. The softest region was the ICHAZ, with values reaching as low as 203 HV_{200} before beginning a steady increase toward the average base metal hardness of 246 HV_{200}. Pattern 3 did not follow this trend. Due to its placement between the two weld beads, this material experienced reheating from deposition of the second weld

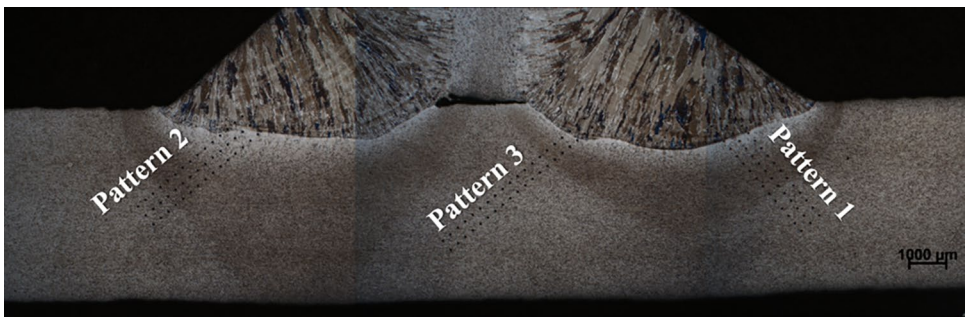

Fig. 19 Composite image of light optical micrographs of the HSLA-80 fillet weld showing placement of microhardness indents. Indents appear as sets of parallel lines of black dots on the left, center, and right sides of the image

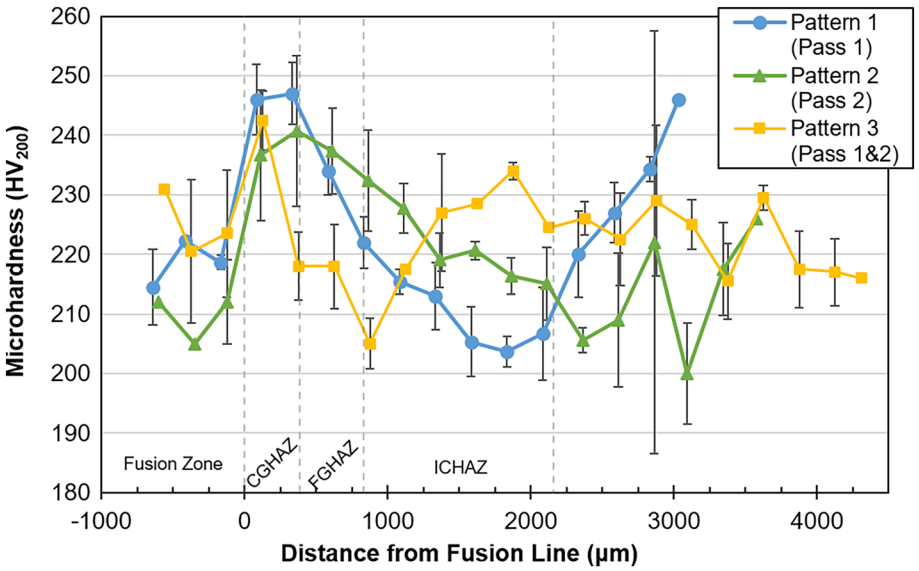

Fig. 20 Average Vickers microhardness across the indents made for each fillet weld pass, as shown in Fig. 19. Error bars are one standard deviation. Values with a negative distance from the fusion line are in the fusion zone. Approximated HAZ regions are delineated by vertical dashed lines

bead and it was difficult to discern a clear pattern over the length of this traverse.

The same analysis was carried out for the butt joint weldment. The fusion zone of the butt joint mirrored that of the tee joint, with a mixture of acicular ferrite, primary ferrite, and unidentified carbides. Heat from the second pass was sufficient to anneal the edge of the fusion zone of the first pass, resulting in polygonal ferrite near the fusion line. Optical micrographs of the HAZ are shown in Fig. 21. Similar microstructures were found in the butt joint and tee joint HAZs. The CGHAZ, shown in Fig. 21a, consisted of bainite and quasipolygonal ferrite. Neither region of the FGHAZ, shown in Fig. 21b–c, showed evidence of bainite. The region adjacent to the CGHAZ consisted of quasipolygonal ferrite and M/A constituent, with more refined ferrite observed in the region adjacent to the ICHAZ. The ICHAZ is shown in Fig. 21d and has a similar microstructural composition as the FGHAZ, with only polygonal ferrite and M/A constituent present. The ferrite grains in the ICHAZ had a much more equiaxed morphology than those in the FGHAZ.

Microhardness testing similar to that reported for the tee joint was performed on the butt joint, with a composite

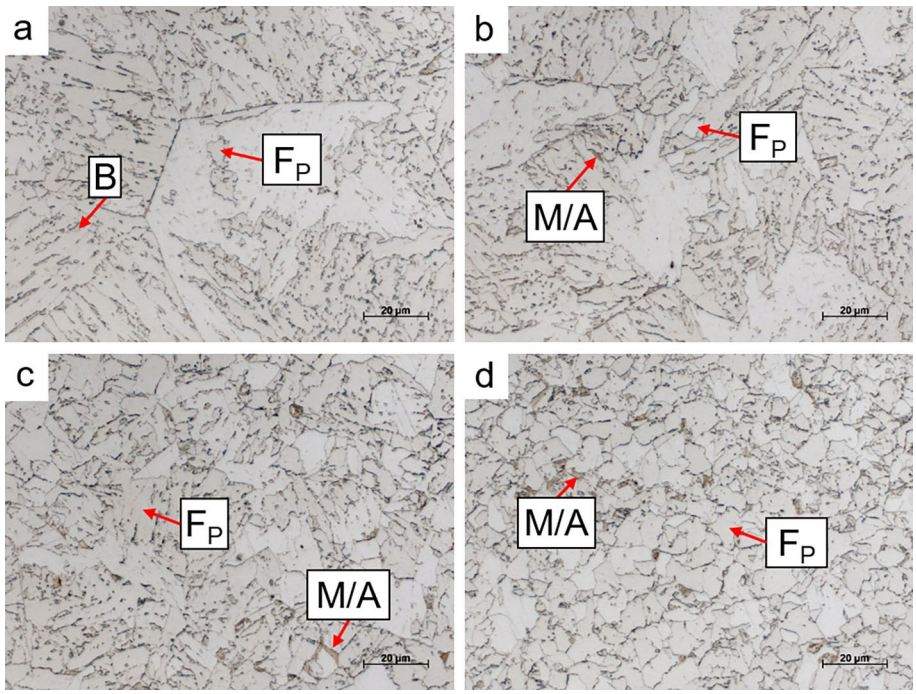

Fig. 21 Representative light optical micrographs of the second pass of the HSLA-80 butt joint showing the **a** CGHAZ, **b** FGHAZ close to the CGHAZ, **c** FGHAZ close to the ICHAZ, and **d** ICHAZ

light optical micrograph shown in Fig. 22 that demonstrates placement of four linear microhardness patterns. Microhardness was assessed near each weld toe in the butt joint, with values presented in Figs. 23 and 24 for the first and second pass, respectively. Microhardness values associated with the first pass were inconsistent between each weld toe due to differences in the extent of reheating done by the second pass. Microhardness pattern 1 followed a similar trend as measurements in the fillet joint, with a relatively high microhardness in the CGHAZ that fell as distance increased into the FGHAZ and ICHAZ before rising again to approach base metal values. Pattern 2 had similar microhardness values in the CGHAZ which also decreased through the ICHAZ, but there was no measured hardness increase in the pattern as it approached the base metal. As shown in the composite micrograph, this is due to the overlap of pattern 2 and the HAZ of the second pass; there is no portion of pattern 2 that reaches true base metal. The microhardness associated with the second pass follows the same pattern as those in the tee joint: relatively high microhardness in both the fusion zone and CGHAZ that dropped through the ICHAZ before increasing again toward base metal values. In general, microhardness values associated with the first pass of the butt joint were softer than those of the second, likely as a result of precipitate dissolution during reheating.

Microhardness values measured in the butt joint were overall slightly lower than those of the tee joint. The butt and tee joints had microhardness ranges of 166–249 and 194–253 HV_{200}, respectively. This is likely due to the differences in heat distribution between the two joint designs. The weld beads in the tee joint are spaced slightly further apart than those in the butt joint. Additionally, the angle of the welding torch used to deposit weld beads resulted in comparatively less overlap in thermal energy distribution. These two geometric factors somewhat isolated the two welded regions from one another in the tee joint configuration. Conversely,

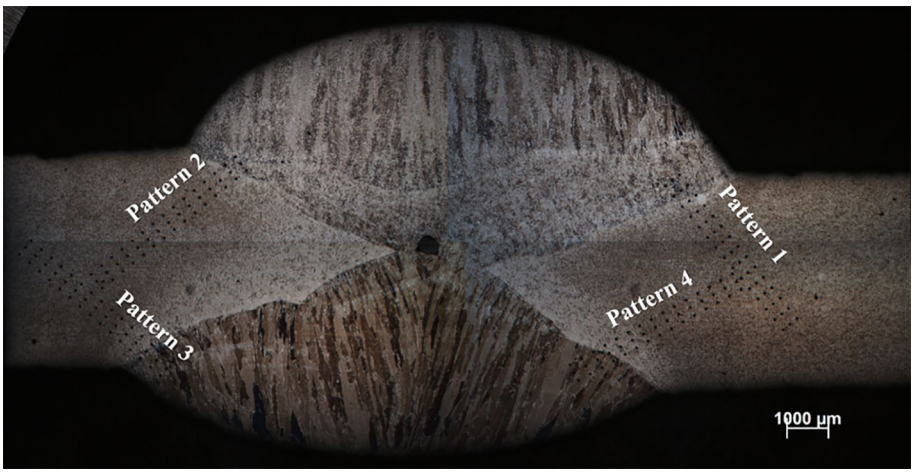

Fig. 22 Composite image of light optical micrographs of the HSLA-80 butt joint weldment showing placement of microhardness indents. Indents appear as three sets of parallel lines of black dots on the left and right sides of the image

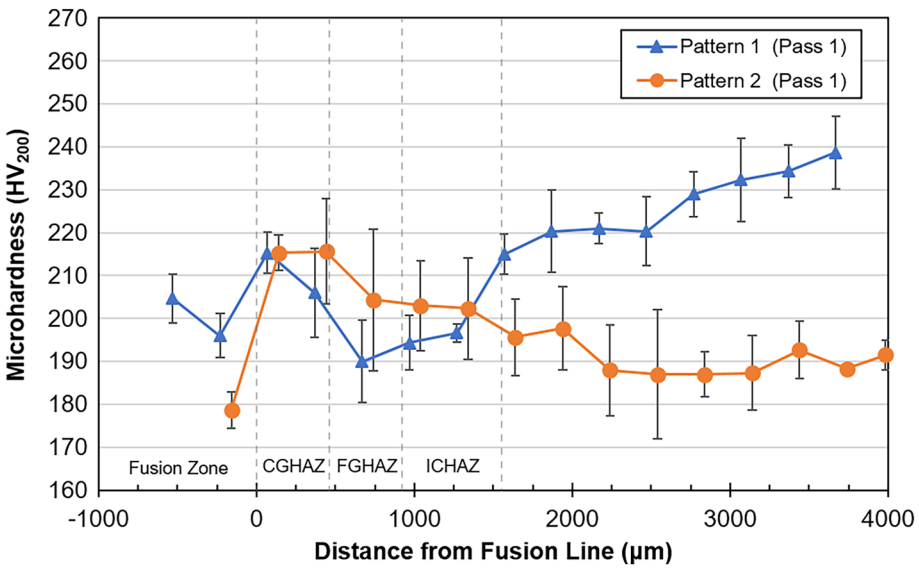

Fig. 23 Vickers microhardness traverses corresponding to the indents shown in Fig. 22 for welding pass 1. Error bars of one standard deviation are shown where two measurements were taken at the same distance from the fusion line

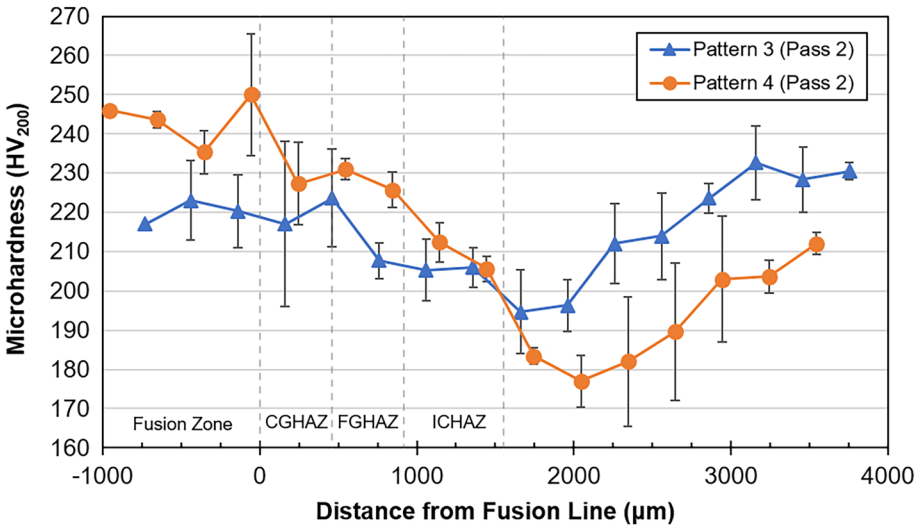

Fig. 24 Vickers microhardness traverses corresponding to the indents shown in Fig. 22 for welding pass 2. Error bars of one standard deviation are shown where two measurements were taken at the same distance from the fusion line

the two weld beads in the butt joint were directly opposite one another, with heat input from the second pass reheating and effectively tempering the first weld bead. The differences in HAZ overlap are apparent in the low magnification images shown in Figs. 19 and 22.

Despite the difference in thermal cycles experienced by each weldment, the observed phases are nominally the same. Increased reheating may have caused a higher degree of precipitate dissolution in the butt joint HAZ, which would have contributed to its lower microhardness without significantly changing phase balance. The HAZ for each joint design can be approximated by Gleeble samples cooled at 10 °C/s (18 °F/s).

Thermo-Physical Property Analysis

The CTE values measured from the dilation curves (n = 5) were $1.5 \times 10^{-5} \pm 1.9 \times 10^{-7}$ °C^{-1} ($8.6 \times 10^{-6} \pm 1.0 \times 10^{-7}$ °F^{-1}) for the untransformed base metal below 650 °C (1202 °F) and $2.2 \times 10^{-5} \pm 9.1 \times 10^{-7}$ °C^{-1} ($1.2 \times 10^{-5} \pm 5.0 \times 10^{-7}$ °F^{-1}) for austenite above 900 °C (1652 °F). A representative graph showing the CTE measurement is given in Fig. 25.

Temperature-dependent density values are shown in Fig. 26. A comparison dataset from a Navy ManTech study [23] conducted at the Naval Metalworking Center from the mid-2000s is also included. The ManTech-generated data are labeled "CTC". Because the slopes of the lines (*i.e.*, the CTE) are nearly identical, differences between the data can be primarily attributed to a difference in the room temperature density measurement techniques used between the two studies. This experimental variation likely exaggerated the difference between the true densities of material from each study.

The measured specific heat and thermal diffusivity data for HSLA-80 can be found in Figs. 27 and 28. The peaks

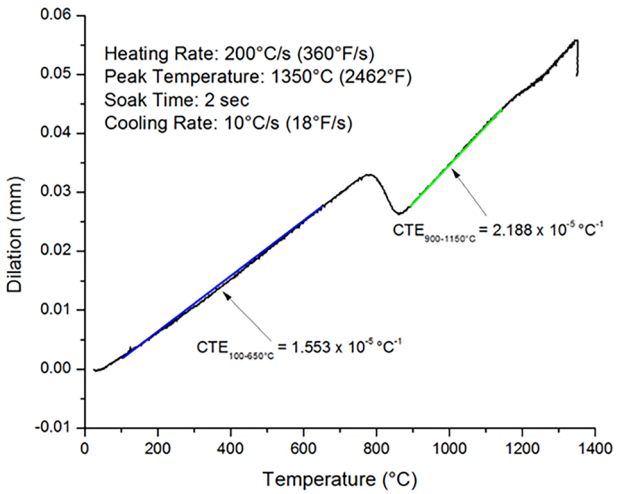

Fig. 25 Representative on-heating dilatometry curve for HSLA-80, showing typical CTE analysis and results

or cusps in the data correspond to the effects of thermal energy absorption during phase transformations, particularly during the austenitic transformation between approximately 700–900 °C (1292–1652 °F). As shown, the data from this study compare very well with the data generated in the Navy ManTech study [23]. The data from Figs. 26, 27, 28 were used in conjunction with Eq. 4 to calculate the temperature-dependent thermal conductivity as shown in Fig. 29. Once again, the data coincides well with the previous reporting from CTC. The raw data points for all of the thermo-physical property graphs can be found in [7].

Thermo-Mechanical Property Analysis

The elevated temperature mechanical testing was performed in accordance with ASTM E21 [13] rather than the stricter

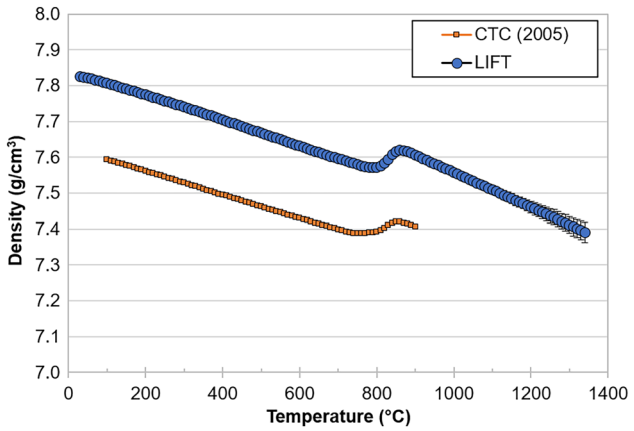

Fig. 26 Density of HSLA-80 steel as a function of temperature. LIFT data measured using analysis of Gleeble-based dilation curves in accordance with Eqs. 2 and 3. CTC data is adapted from reference [23]. Error bars on LIFT data are one standard deviation from the mean of five tests

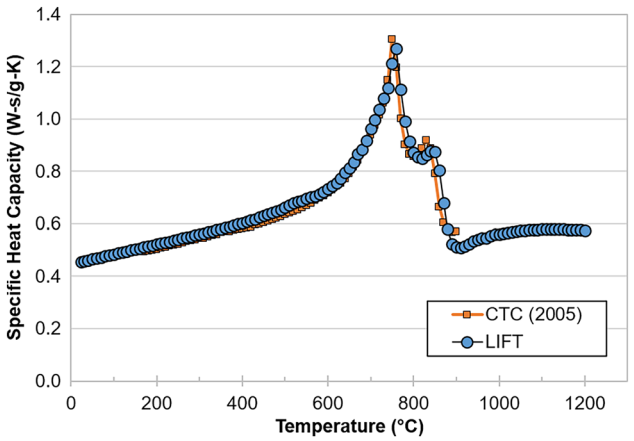

Fig. 27 Measured specific heat for HSLA-80 steel at various temperatures. CTC data adapted from reference [23]

ASTM E111 [45], which is prescribed when elastic modulus measurements are to be made. As such, it was determined that the experimentally measured elevated temperature elastic moduli were likely inaccurate. In order to provide elevated temperature modulus values for a HSLA-80 property database, the data in Fig. 30 were adapted from the European standard for fire design of steel structures [46, 47]. Of the potential sources for this information, the European standard contained the most complete data covering temperatures relevant to this study. Of the potential sources for this information, the European standard contained the most complete data covering temperatures relevant to this study. A room temperature elastic modulus of 210 GPa (30.5 Msi) was assumed [46], as it had been previously for DH36 [5] and HSLA-65 [6] steel. It was also assumed that rigorously

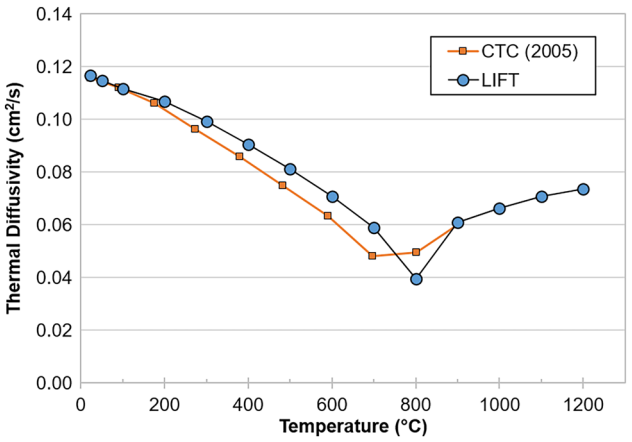

Fig. 28 Measured thermal diffusivity for HSLA-80 steel at various temperatures. CTC data adapted from reference [23]

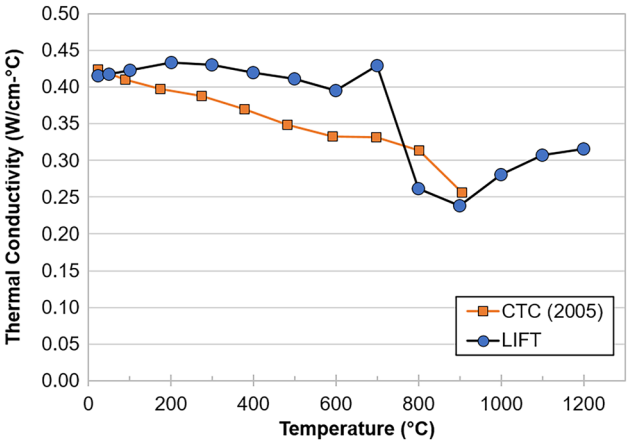

Fig. 29 Calculated thermal conductivity for HSLA-80 steel at various temperatures. CTC data adapted from reference [23]

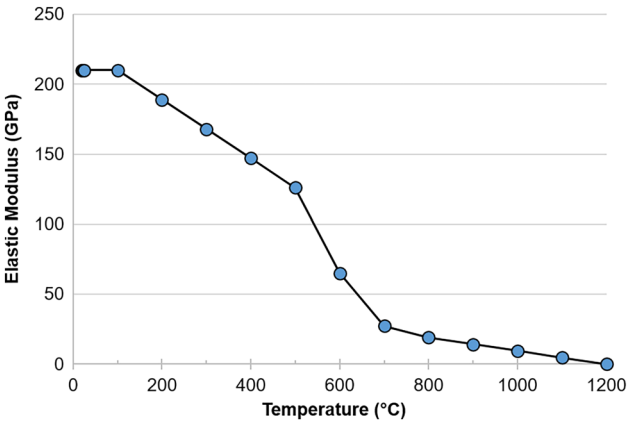

Fig. 30 Assumed elevated temperature elastic modulus for HSLA-80 steel as adapted from references [46, 47]

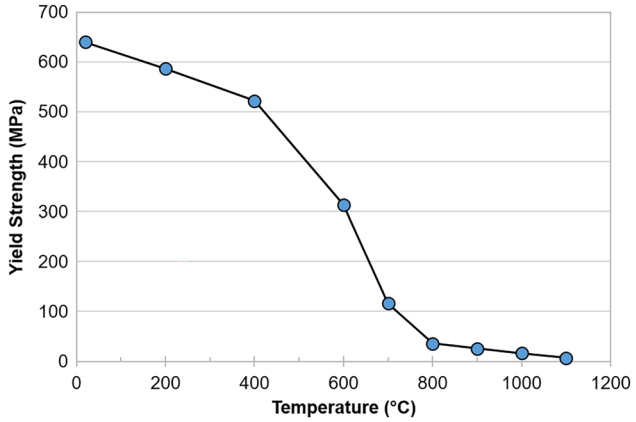

Fig. 31 Measured elevated temperature 0.2% offset yield strength for HSLA-80 steel

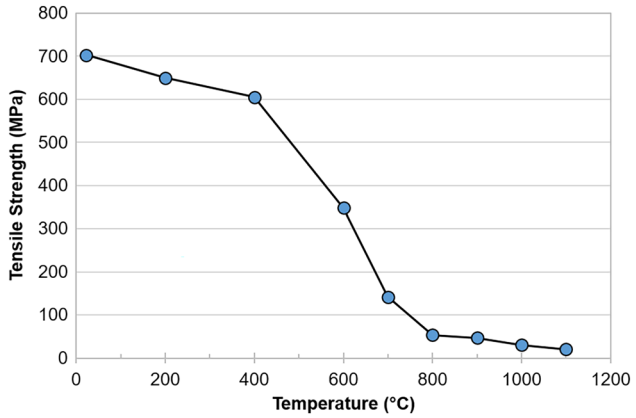

Fig. 32 Measured elevated temperature ultimate tensile strength (UTS) for HSLA-80 steel

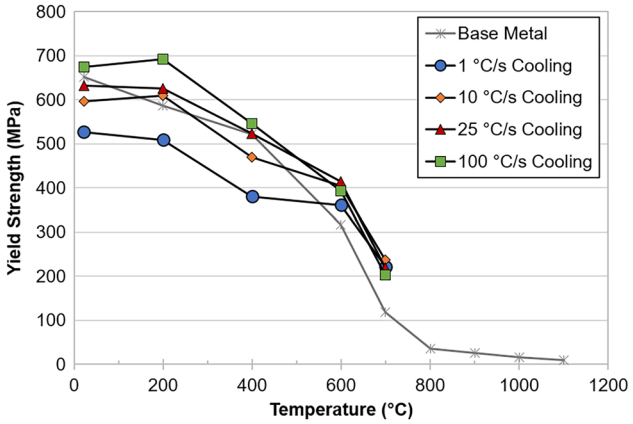

Fig. 33 Yield strength of simulated HSLA-80 CGHAZs after heating to 1350 °C (2462 °F) and cooling at different rates as compared with base material yield strength

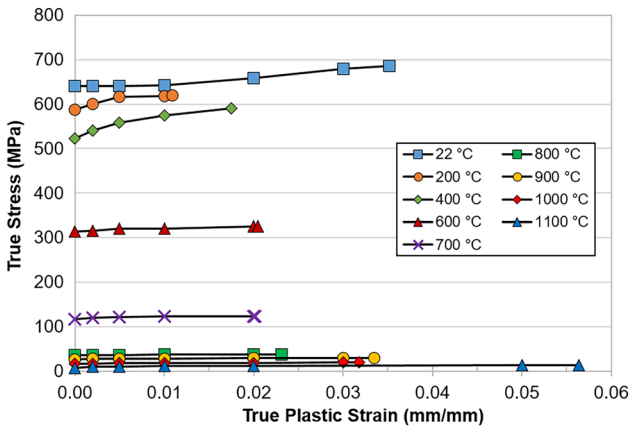

Fig. 34 Elevated temperature flow stress behavior for HSLA-80 steel base material

measured elastic moduli for HSLA-80 steel would be very similar to data presented in Fig. 30 because elastic properties tend to be consistent within a given material class (*e.g.*, low alloy steel). Figure 31 shows the experimentally measured temperature-dependent 0.2% offset yield strength for HSLA-80 base material, and Fig. 32 shows the measured temperature-dependent ultimate tensile strength (UTS). As expected, increased temperatures result in significant strength loss. At temperatures above 800 °C (1472 °F), the base metal microstructure is completely transformed to the weaker austenite phase, resulting in only minor differences in strength with increasing temperature.

Figure 33 shows the measured 0.2% offset yield strengths from specimens cycled to a peak temperature of 1350 °C (2462 °F) along with that of the base material yield strength for comparison. The stress–strain curves associated with the data are given in [7]. At room temperature, only the yield strength of the 100 °C/s (180 °F/s) specimen exceeded that of the base material. This is the result of the formation of a martensitic microstructure as opposed to the ferritic microstructure of the base material. For testing temperatures below 600 °C (1112 °F), an increase in cooling rate was associated with higher yield strength. At room temperature the yield strength of the specimen cooled at 100 °C/s (180 °F/s) was 28% higher than the sample cooled at 1 °C/s (1.8 °F/s). While the base material experienced a distinct decrease in strength as testing temperature increased, the yield strength of thermally cycled specimens changed very little between the 22 °C and 200 °C (72 and 392 °F). For all temperatures higher than 200 °C (392 °F), strength decreased as testing temperature increased until values converged at the 600 °C (1112 °F) testing temperature.

Elevated temperature flow stress measurements for the HSLA-80 base material are shown in Fig. 34 for all temperatures, and Fig. 35 highlights the flow behavior for tests at temperatures of 800 °C (1472 °F) and above. The raw data for these graphs can be found in [7]. The data are true

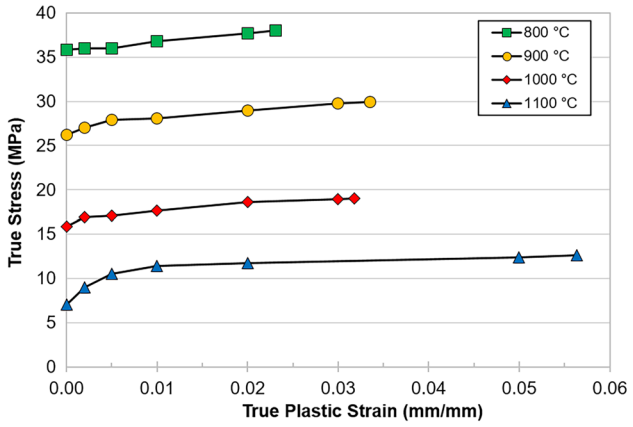

Fig. 35 Elevated temperature flow stress behavior for HSLA-80 steel base material at test temperatures above the austenitic phase transformation

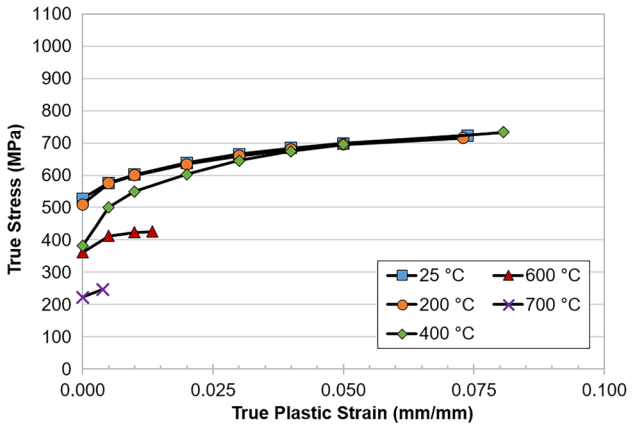

Fig. 36 Flow stress behavior at various temperatures for HSLA-80 steel after cooling at 1 °C/s (1.8 °F/s) from a peak temperature of 1350 °C (2462 °F). Terminal data points are at the UTS

stresses and strains calculated by applying the traditional conversion equations to engineering stress–strain data provided by the test lab. Extensometers were used through yield, but for the protection of laboratory equipment, they were removed from each specimen between 2.0 and 5.7% strain at the discretion of the testing personnel. For all cases this removal occurred well before UTS was reached. As a result, the flow stress behavior is not fully characterized for those samples. It is possible, however, to extrapolate the work hardening behavior to the onset of necking using the UTS values. As expected, increasing the test temperature tends to flatten the flow stress curves, since work hardening is made more difficult by dynamic recovery and/or recrystallization effects.

Flow stress curves for the thermally cycled HSLA-80 are given in Figs. 36, 37, 38, 39. Since these tests were performed under inert atmosphere at NSWCCD, the extensometer

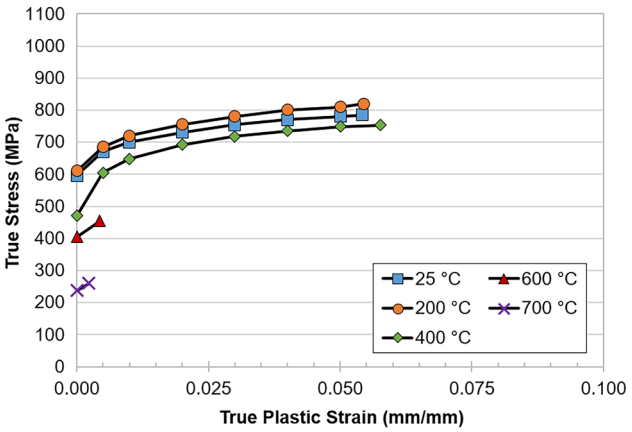

Fig. 37 Flow stress behavior at various temperatures for HSLA-80 steel after cooling at 10 °C/s (18 °F/s) from a peak temperature of 1350 °C (2462 °F). Terminal data points are at the UTS

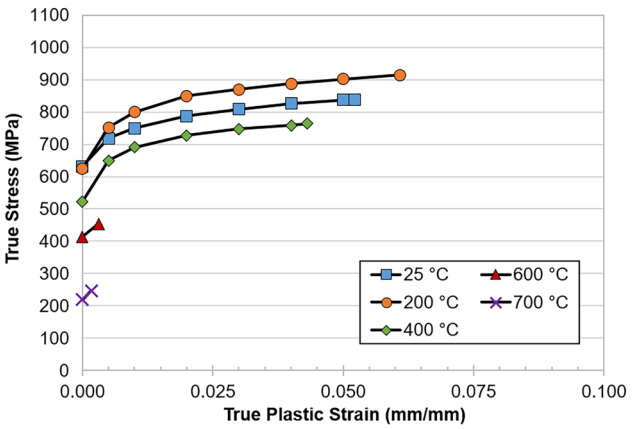

Fig. 38 Flow stress behavior at various temperatures for HSLA-80 steel after cooling at 25 °C/s (45 °F/s) from a peak temperature of 1350 °C (2462 °F). Terminal data points are at the UTS

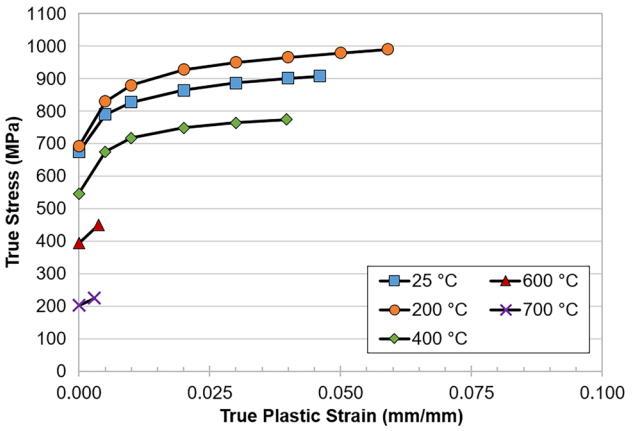

Fig. 39 Flow stress behavior at various temperatures for HSLA-80 steel after cooling at 100 °C/s (180 °F/s) from a peak temperature of 1350 °C (2462 °F). Terminal data points are at the UTS

was not removed during the tests, and more complete flow stress information is available. Once again, the data are true stresses and strains calculated by conversion from engineering stress–strain data. Such conversions are invalid past the onset of necking, so the terminal data points in Figs. 36, 37, 38, 39 are at the UTS. All raw data for these charts, along with the engineering fracture strains for the specimens, are found in [7].

Summary

Temperature-dependent material property data of a pedigreed plate of HSLA-80 steel from room temperature up to nearly the steel's melting point were determined. The thermophysical properties investigated include specific heat, thermal diffusivity, thermal conductivity, CTE, and density. Thermomechanical properties including yield strength, UTS, and flow stress were also measured. The temperatures associated with on-heating and on-cooling phase transformations and their variation with heating rate, cooling rate, and peak temperature were determined and used to develop welding-focused CCT diagrams. Investigation of HAZ microstructures from the CCT specimens and arc welds concluded the analysis. This effort is essential for increasing the fidelity of finite element models used to predict welding-induced distortion and residual stress in marine structures. The data generated in this program are provided to ESI for immediate incorporation into their *SYSWELD* software. The raw datasets of the collected data was uploaded to the University of Michigan's *Materials Commons* data repository at [7]. Should other research groups want to expand on the provided data for HSLA-80, reach out to the corresponding author (C.R. Fisher) as un-used plate material is being stored at NSWCCD in preparation for future efforts.

Acknowledgments The work was funded by the Office of Naval Research (ONR) and the Office of the Secretary of Defense (OSD), in support of the Lightweight Innovations for Tomorrow (LIFT) Institute's program entitled, *Robust Distortion Control Methods and Implementation for Construction of Lightweight Metallic Structures*. The authors would like to thank Huntington Ingalls Industries—Ingalls Shipbuilding for supplying the steel material tested for this program, as well as all team members who worked on the LIFT Joining-R1-3 program.

Declarations

Conflict of interest On behalf of all authors, the corresponding author states that there is no conflict of interest.

References

1. Andersen LF (2000) Residual stresses and deformations in steel structures. Doctoral Thesis, Department of Naval Architecture and Offshore Engineering, University of Denmark
2. MIL-S-22698C (1988) Military specification: steel plate, shapes, and bars, weldable ordinary strength and higher strength: structural, 29 June 1988
3. ASTM A945/M-16 (2016) Standard specification for high-strength low-alloy structural steel plate with low carbon and restricted sulfur for improved weldability, formability, and toughness. ASTM International, West Conshohocken, PA
4. NAVSEA Technical Publication T9074-BD-GIB-010/0300 Rev. 2 (2012) Base materials for critical applications: requirements for low alloy steel plate, forgings, castings, shapes, bars, and heats of HY-80/100/130 and HSLA-80/100, 18 December 2012.
5. Bechetti DH, Semple JK, Zhang W, Fisher CR (2020) Temperature-dependent material property database for marine steels—part 1: DH36. Integr Mater Manuf Innov 9:257–286
6. Semple JK, Bechetti DH, Zhang W, Fisher CR (2022) Temperature-dependent material property databases for marine steels—part 2: HSLA-65. Integr Mater Manuf Innov 11:13–40
7. Fisher CR, Semple JK, Bechetti DH, Zhang W (2022) Temperature-dependent material database: HSLA-80. 11 July 2022. https://doi.org/10.13011/m3-cz82-dw37.
8. ASTM E417-17 (2017) Standard test method for analysis of carbon and low-alloy steel by spark atomic emission spectrometry. ASTM International, West Conshohocken, PA
9. Eisler GR, Fuerschbach PW (1997) SOAR: an extensible suite of codes for weld analysis and optimal weld schedules. In: Seventh international conference on computer technology in welding, San Francisco, CA
10. ASTM E1461-13 (2013) Standard test method for thermal diffusivity by the flash method. ASTM International, West Conshohocken, PA
11. ASTM E1269-11 (2018) Standard test method for determining specific heat capacity by differential scanning calorimetry. ASTM International, West Conshohocken, PA
12. ASTM A370-18 (2018) Standard test methods and definitions for mechanical testing of steel products. ASTM International, West Conshohocken, PA
13. ASTM E21-17 (2017) Standard test methods for elevated temperature tension tests of metallic materials. ASTM International, West Conshohocken, PA
14. Huang TD, Harbison M, Scholler S, Rucker H, Hu J, Dong P, Collette M, Chung H, Groden M, Zhang W, Semple J, Kirchain R, Roth R, Bustamante M, Yang Y, Dull R, Gooroochurn Y, Doroudian M, Fisher CF, Sinfield M, Kihl D, Gonzalez A (2016) Robust distortion control methods and implementation for construction of lightweight metallic structures. SNAME Trans
15. Hehemann RF, Kinsman KR, Aaronson HI (1972) A debate on the bainite reaction. Metall Trans 3:1077–1094
16. Aaronson HI, Spanos G, Reynolds WT (2002) A progress report on the definitions of bainite. Scripta Mater 47(3):139–144
17. Aaronson HI, Enomoto M, Lee JK (2010) Mechanisms of diffusional phase transformations in metals and alloys. CRC Press, Boca Raton
18. Easterling K (1992) Introduction to the physical metallurgy of welding, 2nd edn. Butterworth-Heinemann, Oxford
19. Na S-H, Seol J-B, Jafari M, Park C-G (2017) A correlative approach for identifying complex phases by electron backscatter diffraction and transmission electron microscopy. Appl Microsc 47(1):43–49
20. Das S, Ghosh A, Chatterjee S, Rao PR (2003) Microstructural characterization of controlled forged HSLA-80 steel by transmission electron microscopy. Mater Charact 50(4–5):305–315
21. Fonda RW, Spanos G (2000) Microstructural evolution in ultra-low-carbon steel weldments—Part I: controlled thermal cycling and continuous cooling transformation diagram of the weld metal. Metall Mater Trans A 31:2145–2153
22. Fonda RW, Spanos G, Vandermeer RA (1994) Observations of plate martensite in a low carbon steel. Scripta Metallurgica et Materialia 31(6)

23. Valencia JJ, Papesch C (2005) Automated thermal plate forming: apparent specific heat and thermal expansion during heating of HSLA-80 and DH-36 steel plates. Naval Metalworking Center as operated by Concurrent Technologies Corporation, Johnstown, PA
24. Yurioka N, Oshita S, Tamehiro H (1983) Determination of necessary preheating temperature in steel welding. Weld J 52(6):147–153
25. ASTM E1382-97 (2015) Standard test methods for determining average grain size using semiautomatic and automatic image analysis. ASTM International, West Conshohocken, PA
26. Heinze C, Pittner A, Rethmeiri M, Babu SS (2013) Dependency of martensite start temperature on prior austenite grain size and its influence on welding-induced residual stress. Comput Mater Sci 69:251–260
27. Shome M, Mohanty ON (2006) Continuous cooling transformation diagrams applicable to the heat-affected zone of HSLA-80 and HSLA-100 Steels. Metall Mater Trans A 37A:2159–2169
28. Taljat B, Radhakrishnan B, Zacharia T (1998) Numerical analysis of GTA welding process with emphasis on post-solidification phase transformation effects on residual stress. Mater Sci Eng A A246:45–54
29. Yue X, Lippold JC, Alexandrox BT, Babu SS (2012) Continuous cooling transformatoin behavior in the CGHAZ of naval steels. Weld J 91(3):67–75
30. Mohanty RR, Fonstein N, Girina O (2011) Effect of heating rate on the austenite formation in low-carbon high-strength steels annealed in the intercricial region. Metall Mater Trans A 42A(12):3680–3690
31. Oliveira FLG, Andrade MS, Cota AB (2007) Kinetics of austenite formation during continuous heating in a low carbon steel. Mater Charact 58:256–261
32. Apple CA, Krauss G (1972) The effect of heating rate on the martensite to austenite transformation in Fe-Ni-C alloys. Acta Mater 20:849–856
33. Bainite Committee of The Iron & Steel Institute of Japan (1992) Atlas for bainitic microstructures, vol 1: continuous-cooled microstructures of low carbon HSLA steels. The Iron & Steel Institute of Japan
34. Bhadeshia HKDH, Honeycombe RWK (2006) Steels: microstructure and properties, 3rd edn. Butterworth-Heinemann, Oxford
35. Sinha AK (1989) Ferrous physical metallurgy. Butterworth Publishers, Boston
36. Thewlis G (2004) Classification and quantification of microstructures in steels. Mater Sci Technol 20:143–160
37. International Institute of Welding (1985) Compendium of weld metal microstructures and properties: submerged-arc welds in ferritic steel. Woodhead Publishing, Cambridge
38. Bhadeshia H (2019) Bainite in steels: theory and practice, 3rd edn. CRC Press, Boca Raton
39. Bhagat A, Pabi S, Ranganathan S, Mohanty O (2004) Aging behaviour in copper bearing high strength low alloy steels. ISIJ Int 44(1):115–122
40. Andersson JO, Herlander T, Hoglund L, Shi PF, Sundman B (2002) Thermo-Calc & DICTRA, computational tools for materials science. Calphad 26:92–101
41. Peet M (2014) Prediction of martensite start temperature. Mater Sci Technol 31(11):1370–1375
42. Kang S, Yoon S, Lee S-J (2014) Prediction of bainite start temperature in alloy steels with difference grain sizes. ISIJ Int 54(4):997–999
43. Capdevilla C, Caballero FG, Garcia de Andres C (2002) Determination of ms temperature in steels: a Bayesian neural network model. ISIJ Int 42:894–902
44. Kirkaldy JS, Venugopalan D (1984) Phase transformations in ferrous alloys. In: Phase transformations in ferrous alloys: proceedings of an international conference, Philadelphia, PA
45. ASTM E111-17 (2017) Standard test method for Young's modulus, tangent modulus, and chord modulus. ASTM International, West Conshohocken, PA
46. E. 1993-1-1 (2005) Eurocode 3: Design of steel structures—Part 1–1: general rules and rules for buildings
47. E. 1993-1-2 (2005) Eurocode 3: Design of steel structures—Part 1–2: general rules—structural fire design